Insights into the role of the layer architecture of Cr-Ti-N based coatings in long-term high temperature oxidation experiments in steam atmosphere

S. Mato[a*], J.C. Sánchez-López[b], J. Barriga[c], F.J. Pérez[a] and G. Alcalá[a*]

[a] Grupo de Investigación de Ingeniería de Superficies y Materiales Nanoestructurados Nº 910627, Universidad Complutense de Madrid, Facultad de Ciencias Químicas, E-28040 Madrid, Spain

[b] Instituto de Ciencia de Materiales de Sevilla (CSIC-US), Avda. Américo Vespucio 49, E-41092 Sevilla, Spain

[c] Fundación Tekniker, Parke Teknologikoa, Iñaki Goenaga 5, E-20600 Eibar, Gipuzkoa, Spain

Abstract

Knowledge on hard coatings has been applied in the energy field extending their use as protecting coatings of steam power generation plants components. The role of the layer architecture of Cr-Ti-N based coatings deposited by reactive cathodic arc evaporation on P92 steel substrates was studied with the focus on their oxidation resistance at 650 ºC in 100% steam atmosphere up to 2000 h. Characterization of the coatings was performed by gravimetry, scanning electron microscopy, electron probe microanalysis, glow discharge optical emission spectroscopy, X-ray diffraction, thermodynamic simulations using the CALPHAD method, Rockwell C indentation and nanoindentation. The layered arrangement improves the oxidation resistance of TiN under the working conditions of steam power plants, as well as the mechanical properties of CrN. The produced architectures performance under the described working conditions boosts the understanding of the processes taking place at high temperature, making possible the

design of optimal coatings combine the best behavior of both nitrides for each specific application, reaching a corrosion protection at high temperature in water vapor comparable to that of CrN and a hardness and Young's modulus as high as those of TiN.

Keywords: coatings' design, steam oxidation, diffusion kinetics, thermal analysis, X-ray diffraction, nanoindentation

*Corresponding authors. E-mail addresses:

Dr. S. Mato: msmatodi@ucm.es, Dr. G. Alcalá: galcalap@ucm.es

1. Introduction

The energy industry is continuously searching for innovative ideas to prolong the service life of the power plants components. The marked tendency to increase the vapor temperature in the turbines, in order to improve the efficiency of energy conversion, is generally limited by the oxidation resistance of the most common materials employed. The high thermal conductivity and low thermal expansion coefficients of ferritic-martensitic steels as P92, as well as their good mechanical properties at high temperature, make them suitable for piping and tubing in boilers of ultra-supercritical plants operating in the temperature range of 650–760°C [1,2]. However, in the presence of a steam atmosphere their oxidation resistance is compromised, since instead of the formation of a protective superficial chromia layer, chromium is lost as part of volatile compounds [3, 4].

On this account, the deposition of protective coatings can rise the durability of ferritic-martensitic steels to that of more expensive materials like austenitic stainless steels or nickel-based alloys. The components of power plants are commonly coated with thick overlays (>20 μm; even 100 μm) to resist a pure steam atmosphere at the above mentioned range of temperatures. These layers are produced by slurries or pack cementation, which form intermetallic compounds with the substrate during the subsequent thermal treatment [5, 6]. A high coating thickness increases the cost and modifies the original dimensions of the supporting component. Here, the possibility of using relatively thin nitride coatings (few μm thick) that combine high hardness and high thermal stability is explored, since these properties combination seems reasonable to drive to the desirable service behavior, a priori. In fact, the broad literature available about the performance of metal nitride based coatings at high temperature in air supports this idea [6, 7]. Despite that, the outcome of the present study is not a trivial

matter, since the presence of water vapor in the oxidation atmosphere can change the oxidation mechanisms taking place, as observed in the case of the steel substrate mentioned above [8-10].

A previous study on the oxidation response of magnetron sputtered CrAl(Y)N based coatings (≈ 15 μm of thickness) at 650 ºC in 100% steam atmosphere had shown their protective capability in these conditions [11]. However, the important role of the diffusion paths developed in their columnar microstructure, inherent to physical vapor deposition techniques, compromises the effectiveness of the coatings. In this regard, the benefits of multi-layered coatings over single layers, thanks to the combination of materials with attractive properties of interest for particular service conditions, have been extensively reported [12-19]. From the mechanical and tribological point of view, hard coatings designed by alternating transition metal nitride layers lead to a significant improvement, since the numerous interfaces hinder crack propagation and dislocation movement [12-14]. Also, from the oxidation resistance perspective, the interruption of the above mentioned columnar structure by a tailored sequence of nitride layers may hinder ionic diffusion involved in high temperature phenomena [15, 16]. For instance, it has been reported that TiN/CrN based coatings with a multi-layered arrangement have shown an improvement compared to the performance of the monolayer counterparts when oxidation is carried out in air [17-19].

The present work studies the feasibility of CrTiN based coatings deposited by reactive cathodic arc evaporation to protect ferritic-martensitic P92 steels from oxidation at 650 ^{o}C in 100% steam atmosphere. The influence of the film architecture design on the oxidation protection capabilities is also investigated. Two multi-layers with different layer sequences were deposited and their oxidation protectiveness were compared with those of TiN and CrN monolayers produced for reference purposes. To our knowledge,

the present work is the first time these nitrides have been combined to study their response under the working conditions of ultra-supercritical steam power generation plants. We have only found two investigations in the literature studying the oxidation resistance of these nitrides in 100% steam atmosphere, but without combining them and with an experimental procedure at much lower temperatures and much shorter exposition times [20, 21]. Thus, we aim to explore the possibility of expanding the functionality of these transition metal nitrides, traditionally employed as protective coating in mechanical components, to the power plant technology sector.

2. *Materials and methods*

2.1. Coating deposition

P92 steel specimens, with dimensions 10×20×3 mm, were cut out of a rolled sheet and prepared by abrasive polishing with SiC paper up to grade 600. The substrate samples were sprayed with a solvent and cleaned in an ultrasonic bath with an alkaline detergent. In order to cover all the surfaces, the samples were drilled at the shortest extreme and a thin wire through the hole helped to hold them in the deposition chamber. Detailed composition of the steel is shown in Table 1. The Cr-Ti-N based coatings were deposited on the P92 substrates by reactive cathodic arc evaporation in a laboratory equipment developed by Tekniker (MIDAS 775). This system has twelve circular evaporators of 100 mm of diameter and a working intensity in the range 60-140 A. For this work, four of them were employed, two of Cr (99.7 %, purity) and two of Ti (99.6 %, purity) using a cathode current of 120 A. Prior to deposition, the specimens were etched using a gas mixture of Ar/H_2 for 30 min. Hydrogen is employed to reduce the possible oxides present on the substrate surface. Substrates were mounted in a 2-fold planetary rotation table, at a distance of 370 mm to the target. A very thin Ti underlayer, below 50 nm thick, was applied to the substrates to enhance the adhesion between the

main coating and the P92 steel substrates. Then, a N_2 flow of 300 sccm was introduced in the chamber resulting in a process pressure of 6×10^{-1} Pa. The nitrogen flow was directed toward the substrates to prevent the formation of CrN on the Cr target and to reduce the risk of producing macroparticles. The multi-layered structure was reached by alternating periods of Ti and Cr evaporation with a constant N_2 flow throughout the deposition procedure. A bias voltage of 30 V (DC-pulsed / 20 KHz) was applied to the substrates during the PVD process. The measured temperatures on the substrates during the process ranged between 450 and 500 ºC. Film thicknesses were estimated using the ball crater micro-abrasion method (Calotest).

Figure 1 shows the schemas of three different layer architectures designed and the optical microscopy images of the crater obtained by Calotest. The three-layer TiN/CrTiN/CrN coating consisted of three layers of nitrides: a layer of TiN at the coating/substrate interface of 1.6 μm of thickness, a broad transition zone formed by CrTiN 6.9 μm thick and a top layer of CrN at the media/coating interface with a thickness of 1.2 μm (Figure 1 a)). The multi-layer coating consisted of eleven alternating films of TiN, CrTiN and CrN as schematized in Figure 1 b). Like in the three-layer coating, the CrN and the TiN layers were of similar thickness, in this particular case approximately 0.5 μm, while a thicker layer of a mixed Cr and Ti nitride of about 1.3 μm was produced between them, except for the outer mixed nitride film, which was about 1.7 μm thick. The overall thickness of both coatings is about 10 μm. The monolithic architecture of the CrN and TiN monolayers is displayed in Figure 1 c). The thickness of these monolayer coatings was approximately 3 μm.

2.2. Mechanical analysis

Hardness and the elastic modulus of the as-deposited coatings were measured with a TriboIndenterTM (Hysitron, USA) using a pyramidal Berkovich tip. In order to avoid size effects and to allow reliable comparison of the results in the different coatings without substrate influence, the tests parameters to be used in all the experiments were chosen to reach a maximum indentation depth below the 10% of the thickness of the thinnest coating [22]. The coatings were tested in the load-controlled mode using a trapezoidal loading function consisting on a 5 s loading segment, 10 s peak-load hold and a 5 s unloading segment. A set of 16 nanoindentations made up of a 4×4 matrix was performed in each specimen. The distance between adjacent indents was kept to 10 μm to make sure the obtained results in each nanoindentation was not affected by the previous measurements. The peak-load used in all the tests was 25 mN. Before the experiments were carried out, the tip geometry was calibrated for the indentation depth range obtained in previous measurements in each coating for this peak-load, using fused quartz as standard material. The hardness and elastic modulus were estimated using the method suggested by Oliver and Pharr [23].

2.3. Adhesion tests

Coating/substrate adhesion strength measurements were performed using the Daimler-Benz Rockwell C indentation tests following the VDI 3198 guidelines [24, 25]. The method, developed by the Union of German Engineers (Verein Deutscher Ingenieure, VDI) uses a standard Rockwell hardness tester fitted with a Rockwell C-type diamond cone tip and applies a 150 kg load. The residual marks are examined in an optical microscope and classified using the HF scale, according to the degree of coating delamination and cracking. The adhesion measurements range from HF1 for the best adhesion to HF6 for coating delamination all around the residual imprint.

The Rockwell indenter used in this work was equipped with a conical diamond tip with an inner angle of 120º and a radius of 0.2 mm. In order to achieve meaningful results, the sample total thickness was in all the cases at least 10 times greater the indentation depth.

2.4. Oxidation tests

Annealing of coated and uncoated P92 substrates was conducted in a horizontal furnace at 650 ºC. This furnace was connected to a second one at the same temperature where injected de-oxygenated water from a closed circuit produced a 100% steam atmosphere. Although the experiments do not take into account pressure or wear effects, the oxidation test conditions simulate at the laboratory scale the operation conditions of ultra-supercritical turbine components at steam power plants in terms of environment. A complete description of the laboratory device employed in the study is available in a previous work of the authors [26].

The oxidation kinetics of the coatings and the bare substrate were investigated at 650 ºC in 100% steam atmosphere up to 2000 h. The rate at which oxidation of the specimens occurs was monitored by periodic mass variation measurements in a five-decimal balance, firstly every 24 h, and later, every 150 h approximately. The oxidation experiments started by introducing all the specimens in a ceramic crucible, and the whole setup into the hot zone of the furnace, which was purged after closing with Ar gas. A constant Ar flow was set until the working temperature of the furnace was reached. Then, the Ar flow was cut off and the steam was allowed to circulate into the first furnace. Every time the specimens were removed from the furnace to be weighted, the steam flow was interrupted as the furnace was switched off, and the Ar gas was allowed to enter to the furnace during cooling and drying for 8 h.

2.5. Characterization of the as-deposited and oxidized specimens

Morphological studies of the coatings were carried out using scanning electron microscopy (SEM) in a JEOL JSM 7600F at 15 kV and a working distance of 15 mm. The samples cross sections were previously prepared by grinding up to grade 4000 and further polishing down to 1 μm diamond paste. Coatings and oxidation scales qualitative analysis was performed by energy dispersive X-ray spectroscopy (EDX).

Crystalline phases were determined by X-ray diffraction (XRD) in a PANalytical X'Pert PRO MRD diffractometer employing the International Centre for Diffraction Data (ICDD) as database. Both, Bragg-Brentano (θ-2θ) and grazing angle ($\alpha = 0.5°$) geometries were employed at 45 kV and 40 mA (Kα1Cu), in the scan range 10º-90º (2θ).

Extensive compositional analyses have been conducted on the specimens after oxidation. Compositional profile characterization of the coating layers was achieved by electron probe microanalysis (EPMA) and by means of the line-scanning mode for Cr, Ti, N, and O. Analyses were accomplished in a JEOL Superprobe JXA- 8900M at 20 kV and 50 nA using a beam diameter of 1.2 μm. Complementary compositional profiles were obtained by glow discharge optical emission spectroscopy (GDOES) employing a Horiba Jobin Yvon RF GD instrument, which operated with power of 40 W, using a 650 Pa Ar plasma with a 4 mm diameter copper anode. The wavelengths of the spectral lines used were 130 nm for O, 149 nm for N, 371 nm for Fe, 365 nm for Ti and 425 nm for Cr.

3. Results

3.1. Mechanical analysis

The hardness and elastic modulus obtained for the four coatings are given in Figure 2. The error bars represent the standard deviations of the measurements in each sample. The two monolithic carbides present the maximum difference for both properties, with hardness values of about 21% higher and Young's modulus of about 30% higher in the TiN monolayer compared to the CrN. The three- and the multi-layer coatings present similar elastic modulus to that of the TiN coating. In contrast, while the hardness of the multi-layer is identical to that of the TiN, the results for the three-layer are in between the values for the two monolayers, i.e. TiN and CrN. We can conclude that, from the mechanical point of view and for the parameters employed in these tests, the properties of the multi-layer and the TiN monolithic coating are exactly alike, while the three-layer presents a modulus like that of the TiN monolayer, and an intermediate hardness to that of both monolayers.

3.2. Adhesion analyses

The Rockwell C indents performed in all the coatings lead to no delamination and very limited crack network around the residual indentation mark. These results correspond to the highest adhesion strength quality HF1 the measuring method provides, as presented in Figure 3. Thus, the four studied systems exhibit strong adherent coatings [24], which is a fundamental property for any industrial application.

3.3. Thermogravimetry

Figure 4 gives the mass change per unit area as a function of time recorded during annealing of the coated and uncoated specimens at 650 ºC in 100% steam atmosphere. The graph presents the total mass change calculated by subtracting the mass measured per unit area after each oxidation interval, from the initial mass per unit area of the as-deposited specimen. Reproducibility of the data was assured by the oxidation of three

specimens of each coating and the represented data are the average of the three measurements. The error bars plotted in the graph correspond to the standard deviation of the measurements at each oxidation time.

The mass gain of the bare substrate increases abruptly at the beginning and then, increases continuously until the end of the oxidation test, following a parabolic curve which is related to the formation of a non-protective thick oxide on the steel surface [27].

The protection conferred by the coatings to the substrate leads to a mass gain which is about two orders of magnitude lower to that of the bare substrate. Nevertheless, the oxidation behavior of the three-layer and the TiN monolithic coatings proceed with a continuous mass gain increment with time, while those of the multi-layer and the CrN monolithic coatings show almost no gain. In the case of the TiN coating, the duration of the oxidation test was shortened, since the mass gain measured in the first 164 h pointed out the oxidation of the coating and the development of a thick and non-protective oxide film on its surface.

3.4. SEM observations

Figure 5 shows representative cross sections micrographs of the oxidized coatings on backscattered electron mode. The detection of backscattered electrons was preferred to enhance the contrast between the individual layers forming the coatings with different chemical compositions. The examination of the steel/coating interfaces demonstrated the good adhesion to the substrate, following its topography without cracks nor delamination. Figure 5 a) shows the micrograph of the three-layer coating, where the three nitride layers are disclosed: the CrN and the TiN layers of thickness of 1.1 and 1.8 μm respectively, and the layer with a mixed Cr and Ti nitride 7.1 μm thick between

them. Figure 5 b) presents the multi-layer coating. The eleven alternating layers are clearly revealed exhibiting different contrasts. The darkest and brightest contrast correspond to the TiN and CrN layers respectively, with similar thicknesses (≈0.5 μm). The mixed CrTiN shows an intermediate brightness of larger thickness (1.3-1.7 μm). Interestingly, aside the obvious differences between both coating architectures (i.e. number and distribution of layers), the three-layer system after polishing exhibits long needle-like features perpendicular to the layer interfaces. These features appeared due to the marked columnar structure of the deposited layers. The multi-layer coating however has a smoother appearance. The alternative sequencing of layers of different chemical composition and lower thicknesses makes difficult the development of the typical columnar structure.

The micrographs of the cross section of the oxidized monolithic CrN and TiN coatings are displayed in Figures 6 a) and 6 b) respectively. A thin layer of few nanometers of thickness is observed in the outermost region of the coating surfaces in Figure 5 a), b) and 6 a) suggesting the presence of an oxide film developed in the annealing process. The CrN monolayer, of approximate thickness of 3.3 μm, did not show evidences of oxidation nor degradation after 2000 h of heat treatment apart from the already mentioned superficial thin oxide layer. Contrarily, the TiN monolayer of similar thickness has developed after only 96 h of oxidation a thick layer of corrosion products on the surface of the coating. The oxide layer formed presents some porosity, especially in the outer two thirds of its thickness. Its chemical analysis by means of EDX reveals different oxygen contents, having the inner layer a lower oxygen concentration that the outer. In discrete areas, the coating has failed locally, exposing the substrate to the vapor atmosphere, which has led to its oxidation. The morphology of the local

breakdown regions of the coating can be observed in the specimen cross section in Figure 7 a), and in a planar top view in Figure 7 b).

3.5. EPMA and GDOES analyses

In order to study the chemical modifications caused in the TiN/TiCrN/CrN coatings due to the thermal treatment in steam atmosphere and paying special attention to the oxide films developed on the surface, compositional profiling techniques such as EPMA and GDOES were employed. To that end, profiles of the as-deposited samples were compared to those obtained for the oxidized specimens.

In Figure 8, the EPMA line scan analyses performed along the cross section surface of the coated samples are shown. The Fe and N profiles determine the extension of the coating and the location of the substrate/coating and coating/atmosphere interfaces. The variations in the Ti and Cr signals reproduce exactly the film architecture of each sample: the maxima of the Ti and Cr profiles correspond to the TiN and CrN layers respectively, while the intermediate values obtained between maxima and minima of both signals correspond to the mixed Ti-Cr nitride layers. Thus, in Figures 8 a) and b) three layers can be identified whereas eleven layers are counted in Figures 8 c) and d). The line scans obtained for the as-deposited and the oxidized samples are very similar in both coating architectures. The O signal discloses an increment at the coating/atmosphere interface in all the samples.

To further study the ionic diffusion processes through the layered coatings at high temperature, GDOES experiments were performed on the oxidized samples and compared to those carried out on the initial films (the latter measured in replica samples using the M775 steel as substrate). The results of the study are shown in Figure 9. As in the EPMA compositional profiles, the Fe and N signals help to locate the coating

interfaces. No outward Fe diffusion is detected at the substrate/coating interface. The slow signal decay is characteristic of GDOES spectra due to mixing of species during the necessary erosion of the surface to obtain the depth profiles. Inward diffusion of O is observed throughout the oxidized coatings, particularly at the outer surfaces. This oxygen enrichment is coincident with the increment in the Ti signal in both coating architectures, coupled with a decay in depth due to the slow solid-state diffusion kinetics under the tested conditions. Clearly, GDOES and EPMA analyses reproduce accurately the number of layers disclosed in the SEM micrographs before and after the oxidation experiments.

3.6. Thermodynamic simulations (CALPHAD method)

In order to obtain a deeper understanding of the processes taking place on the outer surface of the coatings during oxidation, thermodynamic simulations were carried out using the CALPHAD method by means of the Thermo-Calc commercial software. The simulations allowed gathering information beyond the detection limit of the characterization techniques available in this work. In all the cases, the outer coating surface/atmosphere interface composition, obtained experimentally, was used as the input of the simulation for each coating.

These analyses have two aims. The first one is to dismiss the formation of gaseous phases containing either Cr or Ti, in order to make sure any measured mass loss is due to solid phases detachment. The second is to understand the effect of the Cr/Ti ratio on the layered coatings' outer surface in the formation of either protective or non-protective oxide films.

Both objectives have been entirely fulfilled, since no gaseous phases containing Cr or Ti have been found to be thermodynamically stable for any of the coatings and, as argued

in the discussion section, the Cr/Ti ratio on the outer surface plays a key role in the solid oxides formed, determining the protective performance of the system under the studied working conditions.

3.7. XRD

Figure 10 displays the XRD diffractograms of the as-deposited and oxidized coatings. The grazing angle geometry has also been used in the case of the oxidized coatings when needed for the identification of the crystalline phases formed on the outermost surface. The patterns obtained for the as-deposited CrN and TiN monolayers reveal the diffraction peaks corresponding to the planes of the face centered cubic NaCl type of the CrN and TiN phases, respectively (Figure 10 a)). The diffraction peaks of the multi-layer coating correspond to the CrN and TiN phases. However, in the case of the three-layer coating, TiN diffraction peaks from the bottom layer could not be detected. The observed diffraction peaks can be assigned to CrN outer film and the broad intermediate CrTiN layer. The peak position between those of the CrN and the TiN suggests the formation of a solid solution of both nitrides.

After oxidation (Figure 10 b)), the diffractograms of the CrN coating in both geometries exhibit peaks characteristics of the Cr_2N and the Cr_2O_3 phases. In the case of the TiN coating, after 164 h of oxidation, the obtained patterns display only diffraction peaks related to oxide phases (TiO_2 and Fe_2O_3). The identification of iron oxide is in agreement with the SEM observations that showed the beginning of the coating failure and the exposure of the substrate to the oxidative atmosphere after only 96 h.

Figure 10 c) shows the diffractograms of the oxidized three- and multi-layer coatings. The patterns obtained with the grazing angle geometry for the three-layer coating after oxidation display peaks mainly related to Cr_2O_3 and the top layer of CrN, although also

the peak at 27.4° indicates the presence of a low content of TiO_2. In the Bragg-Brentano pattern only diffraction maxima related with the CrN and the mixed CrTiN layer are observed. The grazing angle diffractogram of the multi-layer coating confirms the existence of Cr_2O_3 and TiO_2 at the surface, in agreement with the GDOES analysis. Additionally, diffractions peaks related to the top CrN layer are also present. In the case of the Bragg-Brentano diffractogram, the main detected phases are TiO_2, CrN and TiN. The presence of a mixed CrTiN layer, as previously discussed, cannot be discarded.

4. Discussion

TiN is one of the most employed films on cutting tools and forming molds due to its high hardness, strength, wear resistance and excellent adhesion to substrates. However, it lacks of thermal stability, which has been traditionally overcome by the addition of alloying elements such Al [10, 28]. On the other hand, CrN has lower hardness compared to that of TiN (21% lower according to our nanoindentation results) but it is one of the dominant high temperature protecting materials due to its superior oxidation resistance. Oxidation of CrN films proceeds with the development of a protective layer of chromium oxide that prevents further oxidation of the surface [29].

With the aim of combining the advantages of monolithic TiN and CrN coatings, several architectures combining both components were prepared by reactive cathodic arc evaporation. A three layers basic arrangement was firstly considered, comprising an inner hard TiN and an outer oxidation resistant CrN layer. An intermediate layer of mixed Cr and Ti nitride was added to enable a gradual chemical transition between them, ensuring a good adhesion and a smooth property transition. Further, to explore the benefits of a multi-layered design, a coating composed by alternating layers of CrN and TiN, with a CrTiN layer between them, was also produced. Their protective capabilities

have been assessed during 2000 h of oxidation in 100% steam atmosphere at 650 ºC. The results have been compared with those obtained in identical conditions for the uncoated substrate and both monolithic coated samples (i.e. a TiN coating and a CrN coating).

Oxidation of the monolithic TiN and CrN coatings proceeds as expected following previous findings in the literature, although at a much faster kinetics compared to its response in air [30, 31]. The TiN coating oxidized extensively after only 96 h, developing a non-protective layer of TiO_2, which results in the degradation of the coating and therefore, the oxidation of the substrate. Those conclusions can be extracted in light of the continuous mass increment with oxidation time, the SEM images, EDX compositional analysis, as well as the XRD patterns of the coating after oxidation. On the other hand, the CrN coating exhibits a high oxidation resistance, with negligible mass gain and no significant morphological modifications after 2000 h of thermal treatment, apart from the development of a protective thin oxide film on the surface that prevents further oxidation of the coating. However, the XRD results evidence that a phase transformation from cubic CrN to hexagonal Cr_2N has occurred. This is important since it is well known that Cr_2N jeopardizes the protective capabilities of the coating. Such transformation during thermal treatments has been commonly regarded as an indication of its thermal stability limitation [31, 32].

Meanwhile, the oxidation resistance observed for the two Cr-Ti-N-based coatings clearly improves the performance of the bare P92 steel in terms of mass variation versus oxidation time. Furthermore, the oxidation protection of the multi-layer coating seems a priori exceptional, suggesting the beneficial effect of a high number of interfaces. Nevertheless, the analysis of the results provided by the complementary characterization

techniques are needed to extract correct conclusions about the oxidation kinetics observed here.

The layered architecture of both coatings is retained after 2000 h of oxidation, as confirmed by the comparison of the compositional profiles obtained by EPMA and GDOES, and the SEM cross sections inspections of the as-deposited and the oxidized specimens. Importantly, no diffusion of iron species has been detected at the coating/substrate interface of any of the coatings. Whereas the quantification of oxygen inward diffusion is usually regarded as an evidence to explore the thermal stability and oxidation resistance of the coatings, the maintenance of the layered architecture, the low mass gain, the absence of damage in the coatings as observed by SEM after oxidation and the intact substrate, evidence their excellent performance. Nevertheless, the multi-layer

coating is expected to show a lower O income measured by EPMA and GDOES compared to the three-layer in view of the thermogravimetry results. However, although no substantial differences have been obtained by EPMA attending to the oxygen signal, the compositional profile by GDOES reveals a significantly higher penetration of this element in the former. The differences between both techniques evidences the high accuracy of GDOES to detect and quantify light elements [33, 34], compared to EPMA.

In the GDOES results of both layered coatings after oxidation, the O signal is coupled to that of Ti, indicating that the TiN layers oxidized readily, as mentioned above. Moreover, the O signal shows varying values depending on the Ti concentration (higher in the TiN layers than in the TiCrN layers) and on the proximity of the layer to the outer surface (higher in the most external Ti containing layers than in the internal ones), as expected due to the slow solid state diffusion kinetics under the studied conditions. It is

a key issue the observation of Ti in the outer surface of the oxidized multi-layer (above 10 at.%), due to outwards diffusion, in contrast with its much lower concentration (below 2 at.%) in the three-layer, as observed by GDOES (cf. Fig. 9b and 9d). The smaller thickness of the outer CrN film in the former (about 3 times smaller), together with its greater Ti concentration in the outer region due to the presence of the first outer TiN film, located at a depth of 2.2 μm from the outer surface, undoubtedly favor this process.

During oxidation superficial oxides develop, identified by XRD as Cr_2O_3 and TiO_2 in both coatings, although in a greater content in the case of the multi-layer since they can be detected also using the Bragg-Brentano geometry (Fig. 10c). Despite the growth of those crystalline oxides, the O inward diffusion has been detected by GDOES for both coatings, as previously mentioned. This is consistent with the behavior observed for the TiO_2 under the studied conditions, since this oxide does not passivate, allowing ionic diffusion through, and thus the continuous oxidation of the material underneath. In spite of this, the kinetics of the process is slow since, as discussed by Yang et al. [30], Cr_2O_3 fills the pores of TiO_2, slowing down the diffusion of O inwards. Nonetheless, accordingly to this lack of protection in the presence of TiO_2, the O concentration on the surface and in the first 3 μm in depth, are higher in the multi-layer than in the three-layer (cf. Fig. 9b and 9d). Additionally, the XRD results allow a qualitative quantification of the O content in the coatings after oxidation and therefore, clarification on this matter. The presence of TiO, in sufficient quantity to be detected by the Bragg-Brentano XRD analysis, in the case of the oxidized multi-layer coating, and the absence of diffractions from any oxide in the three-layer, indicates unambiguously the higher O content in the interior of the former. This contrasts with the good thermogravimetry results obtained for the multi-layer coating mentioned above. At this point it is worth

mentioning that the nature of the titanium oxide formed on the surface of the coating (TiO_2) differs from that formed in the interior, since the availability of O in the surface ensures the development of an oxide richer in this element. Thus, in light of this discussion, it is plausible that a continuous detachment of the loose TiO_2 formed at the surface of the multi-layer during oxidation occurs, assisted by the presence of steam and the thermal cycles carried out during the experiments. The lost material would mask the mass gain with oxidation time being the actual measured values lower to those expected. The quantification of the lost TiO_2 material is difficult, but we can conclude that its mass should be similar to that of the O trapped within the coating due to inwards diffusion, since the mass gain measured during thermogravimetry after 2000 h is negligible. However, the lower Ti concentration in the outer regions of the three-layer, more than 5 times lower according to our GDOES results, leads to a reduced formation of TiO_2 on the surface, not being enough to observe mass losses but still allowing some O inwards diffusion.

In order to obtain a deeper understanding of the processes taking place on the surface of the layered coatings, two thermodynamic simulations were developed using the at.% concentrations of the elements present on the surfaces of each sample as obtained by GDOES, with excess of the steam atmosphere and as a function of temperature. The outcomes of the simulations are consistent with the experimental results, predicting the formation of TiO_2 and Cr_2O_3 on the outer surface of both coatings at 650 ºC, as the only thermodynamic stable solid phases, which agrees with the grazing angle XRD analyses after oxidation. Nevertheless, the simulations show additional information not noticed experimentally. Although the compounds obtained are the same in both specimens, the two cases differ as a function of the proportion between Cr and Ti on the surface. When the amount of Cr is much greater than that of Ti, like in the case of the three-layer

coating, Cr_2O_3 admits nearly 0.5 at.% Ti in solid solution at 650 ºC in the form of $(Cr,Ti)_2O_3$, which reduces the amount of the non-protective TiO_2 on the outer surface of the layered coatings. If we consider that the concentration of Ti on the outer surface of this sample, as measured by GDOES, is below 2 at.%, the obtained solubility becomes relevant in the overall performance of the coating, favoring the formation of a protecting oxide at the expense of a non-protective one. It is also remarkable that while maintaining the ratio Cr/Ti, the solubility of Ti in Cr_2O_3 raises with temperature, up to a point that TiO_2 does not form. This suggests that if this ratio is kept constant, the system should increase its oxidation resistance at temperatures above 650 ºC. However, at higher temperatures the kinetics of diffusion processes rises, making difficult to hold a propitious Cr/Ti ratio on the outer sample surface.

Contrarily, when the concentration of Ti approaches that of Cr, like in the case of the multi-layer coating, the formation of TiO_2 becomes thermodynamically more stable than the dissolution of Ti in Cr_2O_3. In this case TiO_2 becomes a stable solid phase for temperatures even above 1500 ºC, which enable O inwards diffusion in the coating.

Also of importance, no evidences of the presence of the hexagonal Cr_2N phase is found in the XRD patterns of the oxidized layered coatings contrarily to that observed in the CrN monolayer. A decrement in the N content, caused likely by the outward diffusion of this element throughout the monolithic coating, necessarily occurs for this phase transformation to take place. The mechanisms to explain how that phenomenon has been hindered in the case of the layered coatings needs further studies, although the presence of Ti enabling O inwards diffusion seems to be behind this behavior. Furthermore, since thermodynamic studies assure the stability of the CrN phase up to annealing temperatures far enough from those employed here [35] kinetics factors are expected to play a key part.

Focusing now on the mechanical properties of the studied coatings, the hardness and elastic modulus of the monolithic TiN and the multi-layer coating are alike, with values of 24 and about 500 GPa respectively. As expected, the monolithic CrN coating presented the lowest hardness and modulus, i.e. 19 and 360 GPa respectively. On the other hand, the three-layer coating shows an intermediate hardness but the same modulus than TiN, 21 and 498 GPa. In order to understand these results it is necessary to consider the thickness of each individual layer in the coating architecture up to a depth of ten times the maximum penetration depth in the nanoindentation tests. In all the experiments, this depth was in the range of 250 to 300 nm, which means the region mechanically tested was in the outer 2.5 to 3 μm of the coatings, with a larger influence of the outer zones.

It is noteworthy the fact that the multi-layer exhibits the same hardness and modulus than the monolithic TiN, although it has an outer CrN layer 0.5 μm thick which is expected to be softer and with a lower modulus than TiN. This can be explained by the sum of several factors. First, the CrTiN below the outer CrN layer is expected to present a higher hardness and modulus than the latter. As reported by Alcalá et al. [22] the effects of deeper regions are more relevant for hardness than for elastic modulus, in comparison with shallower zones of the tested material. Second, the absence of a columnar structure due to the interruption of the film deposition in the multi-layer, drives to a more compact film compared to the three-layer, which increases stiffness. Finally, the CrN/CrTiN interface acts as a dislocation barrier, leading to a lower plastic strain during the tests and consequently to a higher hardness [12]. Thus, the architecture of the coating plays an important role not only in the high temperature oxidation resistance, but also in the mechanical response, allowing the optimization of the

combination of CrN and TiN properties in the specific layered design for tailored applications.

Concerning the tri-layered architecture, the outer CrN film is about 1.2 μm thick, which means a larger influence of this layer is expected in this system compared to the multi-layer. The lower hardness obtained for this system relates to the lower influence of the CrTiN underneath and the larger distance of the interface from the material plastic flow during nanoindentation. However, the measured modulus is maintained due to the still low flaw density in the outer CrN film, together with the effect of the underneath mixed nitride influence, although in a lower extent.

5. *Conclusions*

The oxidation resistance of two CrN/CrTiN/TiN coatings with different architectures (three- and multi-layered) has been for the first time assessed and compared to that of single layers of CrN and TiN under the temperature and atmosphere working conditions of ultra-supercritical vapor turbines (650 ºC in 100% steam atmosphere). Both architectures display an excellent oxidation resistance comparable to that of the CrN monolithic coating, which is far better than that of the bare steel and of the TiN coating. The presence of Ti in the layered coatings leads to the formation of a mixed Cr_2O_3 and TiO_2 film on the outer surface, that although protects the coating from degradation allows some O inwards diffusion through. This process is linked to the amount of TiO_2 in this external film which in turn depends on the concentration of Ti on the outer surface. Despite the detected O within the coating, the original layered architecture is kept after 2000 h of exposition to the working conditions, without any damage observed neither in the coating nor in the substrate. The presence of O within the film, as measured by GDOES, seems to counteract the loss of N due to outwards diffusion,

responsible for the undesirable phase transformation from cubic CrN to hexagonal Cr_2N observed in the monolithic CrN coating. In order to determine which of these processes has a slower kinetics and thus which coating has a longer life in service, further work should be carried out exposing the coatings at the operation conditions for periods longer than 2000 h.

Additionally, despite the presence of CrN in the layered architectures, their Young's moduli and hardnesses of the layered coatings is like that of the single TiN, but the three-layer coating which presents a hardness in between that of both nitrides.

The understanding achieved in this work about the diffusion processes taking place in alternating CrN/CrTiN/TiN at the working conditions of ultra-supercritical steam power plants, and the influence of each layer and their interfaces on the mechanical properties of the coatings, allows optimizing the best coating architecture for tailored application, either for high temperature oxidation in steam atmosphere, for hard coatings or for mixed working conditions. The position of each layer within the coating architecture and their thickness are the key issue to achieve the desired performance in service.

Funding

This work was supported by the European Regional Development Funds Program (EU-FEDER) and the Spanish Ministry of Economy, Industry and Competitiveness (projects n° MAT2015-65539-P and MAT2015-69035-REDC).

References

[1] J.C. Vaillant, B. Vandenberghe, B. Hahn, H. Heuser, C. Jochum, T/P23, 24, 911 and 92: New grades for advanced coal-fired power plants—Properties and experience, Int. J. Press. Vessels Pip. 85 (2008), 38, http://dx.doi.org/10.1016/j.ijpvp.2007.06.011

[2] Advanced Coal Technologies: Greater Efficiency and Lower CO_2 Emissions, National Coal Council, Inc. (Report requested by the USA Secretary of Energy - 2008), http://www.nationalcoalcouncil.org/Documents/Advanced_Coal_Technologies.pdf (Last accessed: August 2020)

[3] J. Yuan, X. Wu, W. Wang, S. Zhu, F. Wang, Investigation on the enhanced oxidation of Ferritic/Martensitic steel P92 in pure steam, Materials 7 (2014) 2772-2783, http://dx.doi.org/10.3390/ma7042772

[4] S.R.J. Saunders, M. Monteiro, F. Rizzo, The oxidation behaviour of metals and alloys at high temperatures in atmospheres containing water vapor: A review, Prog. in Mater. Sci. 53 (2008) 775–837, http://dx.doi.org/10.1016/j.pmatsci.2007.11.001

[5] C. Boulesteix, V. Kolarik, F. Pedraza, Steam oxidation of aluminide coatings under high pressure and for long exposures, Corrosion Sci. 144 (2018) 328–338, https://doi.org/10.1016/j.corsci.2018.08.053

[6] D. Schmidt, M.C. Galetz, M. Schütze, Ferritic-martensitic steels: improvement of the oxidation behavior in steam environments via diffusion coatings, Surf.

Coat. Technol. 237 (2013) 23–29, https://doi.org/10.1016/j.surfcoat.2013.09.018

[7] P.H. Mayrhofer, H. Willmann, C. Mitterer, Oxidation kinetics of sputtered Cr–N hard coatings, Surf. Coat. Technol. 146–147 (2001) 222–228, http://dx.doi.org/10.1016/S0257-8972(01)01471-2

[8] L. Cunha, M. Andritschky, K. Pischow, Z. Wang, A. Zarychta, A.S. Miranda, A.M. Cunha, Performance of chromium nitride and titanium nitride coatings during plastic injection moulding, Surf. Coat. Technol. 153 (2002) 160–165, http://dx.doi.org/10.1016/S0257-8972(01)01690-5

[9] Z. Gao, Y. Chen, J. Kulczyk-Malecka, P. Kelly, Y. Zeng, X. Zhang, C. Li, H. Liu, N. Rohbeck, P. Xiao, Comparison of the oxidation behavior of a zirconium nitride coating in water vapor and air at high temperature, Corrosion Sci. 138 (2018) 242–251, https://doi.org/10.1016/j.corsci.2018.04.015

[10] Z. Wang, X. Li, W. Li, P. Ke and A. Wang, Comparative study on oxidation behavior of Ti_2AlN coatings in air and pure steam, Ceram. Int. 45 (2019) 9260-9270, https://doi.org/10.1016/j.ceramint.2019.02.004

[11] S. Mato, G. Alcalá, M. Brizuela, R. Escobar Galindo, F.J. Pérez, J.C. Sánchez-López, Long-term high temperature oxidation of CrAl(Y)N coatings in steam atmosphere, Corrosion Sci. 80 (2014) 453–460, http://dx.doi.org/10.1016/j.corsci.2013.11.066

[12] S.J. Bull, A.M. Jones, Multilayer coatings for improved performance, Surf. Coat. Technol. 78 (1996) 173–184, http://dx.doi.org/10.1016/0257-8972(94)02407-3

[13] D. Yin, X. Peng, Y. Qin, Z. Wang, Impact of residual stress on the adhesion and tensile fracture of TiN/CrN multi-layered coatings from first principles, Phys. E 44 (2012) 1838–1845, http://dx.doi.org/10.1016/j.physe.2012.05.008

[14] A. Lousa, J. Romero, E. Martínez, J. Esteve, F. Montalà, L. Carreras, Multilayered chromium / chromium nitride coatings for use in pressure die-casting, Surf. Coat. Technol. 146 –147 (2001) 268–273, http://dx.doi.org/10.1016/S0257-8972(01)01476-1

[15] L. Chen, Y.X. Xu, Y. Du, Y. Liu, Effect of bilayer period on structure, mechanical and thermal properties of TiAlN/AlTiN multilayer coatings, Thin Solid Films 592 (2015) 207–214, http://dx.doi.org/10.1016/j.tsf.2015.09.029

[16] P. Ren, S. Zhu, F. Wang, Microstructure and oxidation behavior of a Ni+CrAlYSiHfN/AlN multilayer coating fabricated by reactive magnetron sputtering, Corrosion Sci. 104 (2016) 197–206, http://dx.doi.org/10.1016/j.corsci.2015.12.012

[17] X.T. Zeng, S. Zhang, C.Q. Sun, Y.C. Liu, Nanometric-layered CrN/TiN thin films: mechanical strength and thermal stability, Thin Solid Films 424 (2003) 99–102, http://dx.doi.org/10.1016/S0040-6090(02)00921-5

[18] C. Liu, A. Leyland, Q. Bi, A. Matthews, Corrosion resistance of multi-layered plasma-assisted physical vapor deposition TiN and CrN coatings, Surf. Coat. Technol. 141 (2001) 164–173, http://dx.doi.org/10.1016/S0257-8972(01)01267-1

[19] P. Panjan, B. Navinsek, A. Cvelbar, A. Zalar, J. Vlcek, High-temperature oxidation of TiN/CrN multilayers reactively sputtered at low temperatures,

Surf. Coat. Technol. 98 (1998) 1497–1502, https://doi.org/10.1016/S0257-8972(97)00395-2

[20] S.S. Raiman, C. Ang, P. Doyle and K.A. Terrani, Hydrothermal Corrosion of SiC Materials for Accident Tolerant Fuel Cladding with and Without Mitigation Coatings, In: Jackson J., Paraventi D., Wright M. (eds) Proceedings of the 18th International Conference on Environmental Degradation of Materials in Nuclear Power Systems – Water Reactors (2019). The Minerals, Metals & Materials Series. Springer, Cham. https://doi.org/10.1007/978-3-030-04639-2_98

[21] S.S. Raiman, P. Doyle, C. Ang, Y. Katoh, K.A. Terrani, Hydrothermal Corrosion of Coatings on Silicon Carbide in Boiling Water Reactor Conditions, Corrosion, 75(2), (2019) 217-223, https://doi.org/10.5006/2997

[22] G. Alcalá. S. Mato, P. Skeldon, G.E. Thompson, A.B. Mann, H. Habazaki, K. Shimizu, Mechanical properties of barrier-type anodic alumina films using nanoindentation, Surf. Coat. Technol. 173 (2003) 293–298, http://dx.doi.org/10.1016/S0257-8972(03)00738-2

[23] W.C. Oliver, G.M. Pharr, An improved technique for determining hardness and elastic modulus using load and displacement sensing indentation experiments, J. Mater. Res. 7 (1992) 1564-1583, http://dx.doi.org/10.1557/JMR.1992.1564

[24] N. Vidakis, A. Antoniadis, N. Bilalis, The VDI 3198 indentation test evaluation of a reliable qualitative control for layered compounds, J. Mater. Process. Technol. 143–144 (2003) 481–485, http://dx.doi.org/10.1016/S0924-0136(03)00300-5

[25] W. Heinke, A. Leyland, A. Matthews, G. Berg, C. Friedrich, E. Broszeit, Evaluation of PVD nitride coatings, using impact, scratch and Rockwell-C adhesion tests, Thin Solid Films 270 (1995) 431–438, http://dx.doi.org/10.1016/0040-6090(95)06934-8

[26] J. Leal, G. Alcalá, F.J. Bolívar, L. Sánchez, M.P. Hierro, F.J. Pérez, Simulation and experimental approach to CVD-FBR aluminide coatings on ferritic steels under steam oxidation, Corrosion Sci. 50 (2008) 1833–1840, http://dx.doi.org/10.1016/i.corsci.2008.03.014

[27] D. Huenert, A. Kranzmann, Impact of oxyfuel atmospheres $H_2O/CO_2/O_2$ and H_2O/CO_2 on the oxidation of ferritic-martensitic and austenitic steels, Corrosion Sci. 53 (2011) 2306–2317, http://dx.doi.org/10.1016/j.corsci.2011.03.015

[28] S. PalDey, S. Deevi, Single layer and multilayer wear resistant coatings of (Ti, Al) N: a review, Mater. Sci. Eng. A 342 (2003) 58–79, http://dx.doi.org/10.1016/S0921-5093(03)00473-8

[29] C. Meng, L. Yang, Y. Wu, J. Tan, W. Dang, X. He, X. Ma, Study of the oxidation behavior of CrN coating on Zr alloy in air, J. Nucl. Mater. 515 (2019) 354-369, https://doi.org/10.1016/j.jnucmat.2019.01.006

[30] K. Yang, B. Liao, H. Zhu, W. Zhu, H. He, Y. Liu, H. Li and X. Wang, Influence of the Cr interlayer on the microstructure of sputtered TiN coatings deposited on zirconium alloy, Mater. Res. Express, 6 (2019) 026420, https://doi.org/10.1088/2053-1591/aaf041

[31] Z.B. Qi, B. Liu, Z.T. Wu, F.P. Zhu, Z.C. Wang and C.H. Wu, A comparative study of the oxidation behavior of Cr_2N and CrN coatings, Thin Solid Films, 544 (2013) 515-520, https://doi.org/10.1016/j.tsf.2013.01.031

[32] E. Mohammadpour, Z.T. Jiang, M.Altarawneh, N. Mondinos, M.M. Rahman, H.N. Lim, N.M. Huang, Z. Xie, Z.F. Zho, B.Z. Dlugogorski, Experimental and predicted mechanical properties of $Cr_{1-x}Al_xN$ thin films, at high temperatures, incorporating in situ synchrotron radiation X-ray diffraction and computational modelling, RSC Adv. 7 (2017) 22094-22104, https://doi.org/10.1039/C7RA00342K

[33] M. Wilke, G. Teichert, R. Gemma, A. Pundt, R. Kirchheim, H. Romanus and P. Schaaf, Glow discharge optical emission spectroscopy for accurate and well resolved analysis of coatings and thin films, Thin Solid Films, 520, (2011) 1660-1667, https://doi.org/10.1016/j.tsf.2011.07.058

[34] G. Gamez and K. Finch, Recent advances in surface elemental mapping via glow discharge atomic spectrometry, Spectroc. Acta Pt. B-Atom. Spectr., 148 (2018) 129-136, https://doi.org/10.1016/j.sab.2018.06.015

[35] P.H. Mayrhofer, F. Rovere, M. Moser, C. Strondl, R. Tietem, Thermally induced transitions of CrN thin films, Scripta Materialia 57 (2007) 249–252, https://doi.org/10.1016/j.scriptamat.2007.03.058

Captions

Figure 1: Schematic layer architecture designs of the coatings and images of craters grinded by ball crater micro-abrasion method (Calotest) of a) three-layered CrN/CrTiN/TiN coating, b) multi-layered CrN/CrTiN/TiN coating and c) monolithic TiN or CrN coating: (Ti,Cr)N).

Figure 2: Young's modulus and hardness of the studied coatings.

Figure 3: Optical micrographs of the residual mark produced after Daimler-Benz Rockwell C indentation adhesion tests on the four studied coatings, and adhesion scale employed (VDI 3198).

Figure 4: Mass change per unit area versus time of the substrate P92 and the coatings under study up to 2000 h at 650 ºC in 100% steam atmosphere. The inset shows an enlargement of the part of the graph corresponding to the three coatings which have shown the lowest mass change.

Figure 5: SEM micrographs, in cross section view, of the oxidized up to 2000 h at 650 ºC in 100% steam atmosphere a) of the CrN/CrTiN/TiN three-layer coating, and b) the CrN/CrTiN/TiN multi-layered coating.

Figure 6: SEM micrographs, in cross section view, a) of the CrN monolithic coating oxidized up to 2000 h, and b) the TiN monolithic coating oxidized up to 96 h. In both cases oxidation took place at 650 ºC in 100% steam atmosphere

Figure 7: SEM micrographs of the TiN monolithic coating oxidized up to 96 h at 650 ºC in 100% steam atmosphere a) in a cross section view showing coating failure, and b) in a planar top view.

Figure 8: Compositional depth profiles by EPMA of as-deposited and oxidized at 650 °C to 2000 h in 100% steam atmosphere: a) and b) CrN/CrTiN/TiN three-layer coating, c) and d) CrN/CrTiN/TiN multi-layer coating.

Figure 9: Compositional depth profiles by GDOES of as-deposited and oxidized at 650 °C to 2000 h in 100% steam atmosphere: a) and b) CrN/CrTiN/TiN three-layer coating, c) and d) CrN/CrTiN/TiN multi-layer coating.

Figure 10: XRD diffractograms of the a) as-deposited coatings with Bragg-Brentano geometry, b) oxidized monolithic coatings with Bragg-Brentano geometry, and c) oxidized layered coatings with Bragg-Brentano (BB) and grazing angle (GA) geometries.

Figure 1a

Click here to download high resolution image

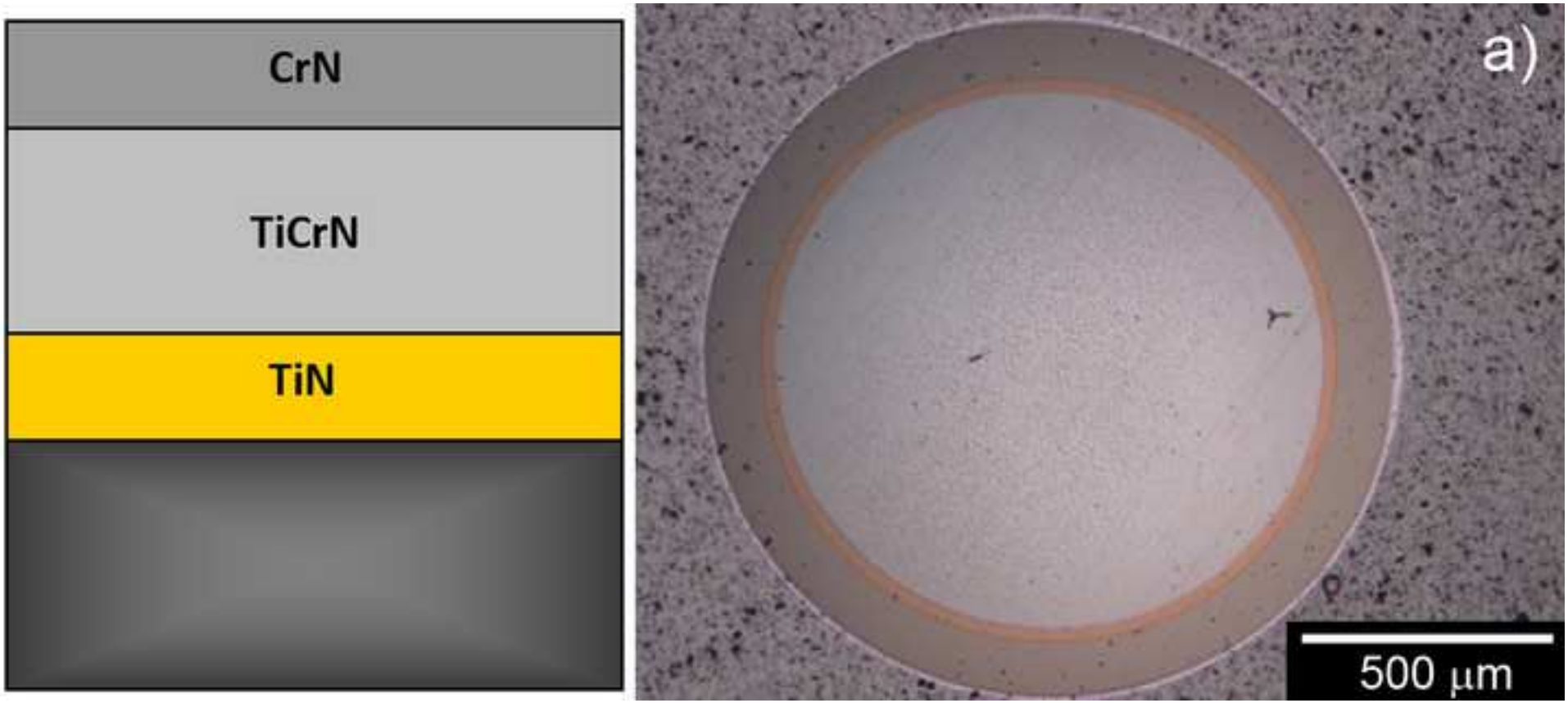

Figure 1b

Click here to download high resolution image

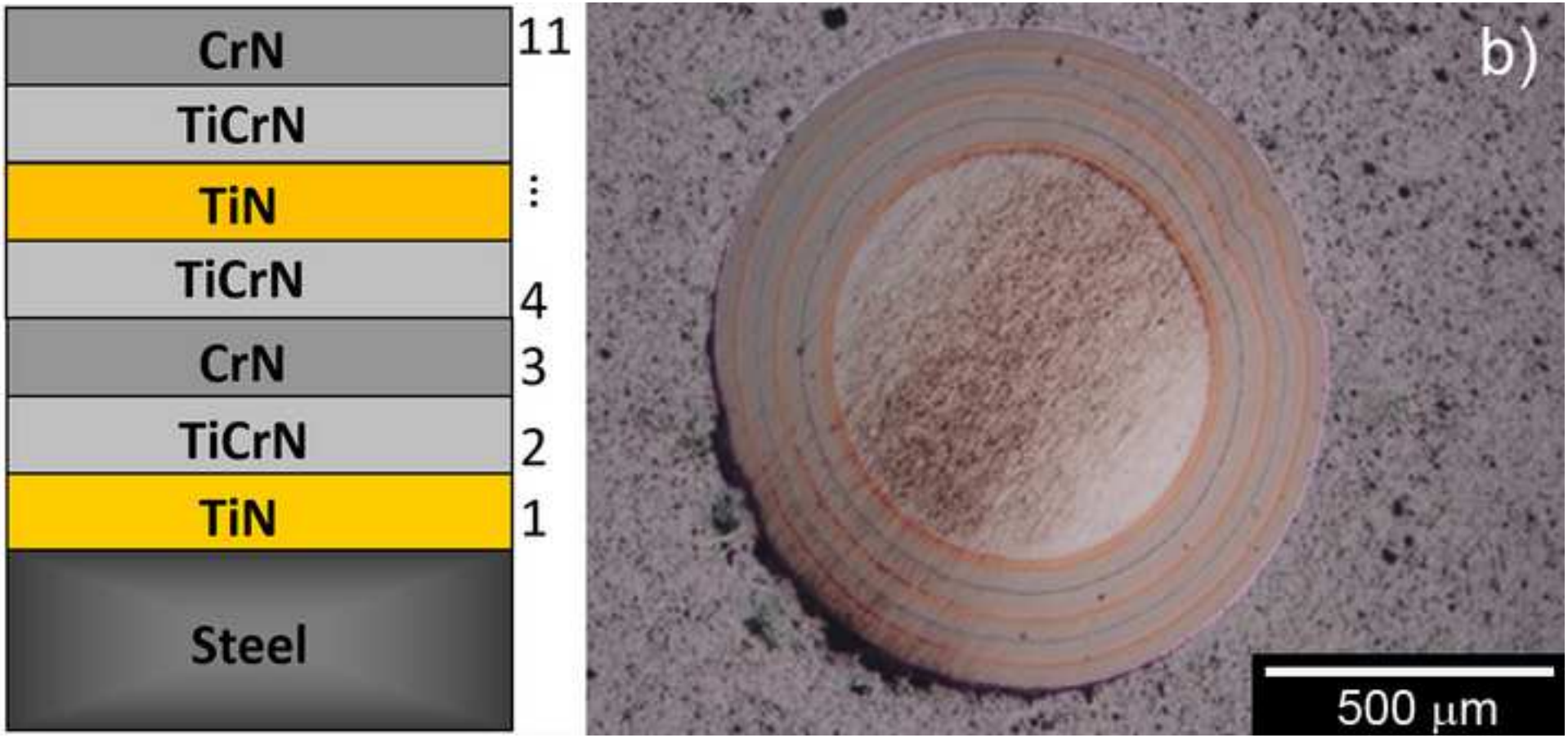

Figure 1c

Click here to download high resolution image

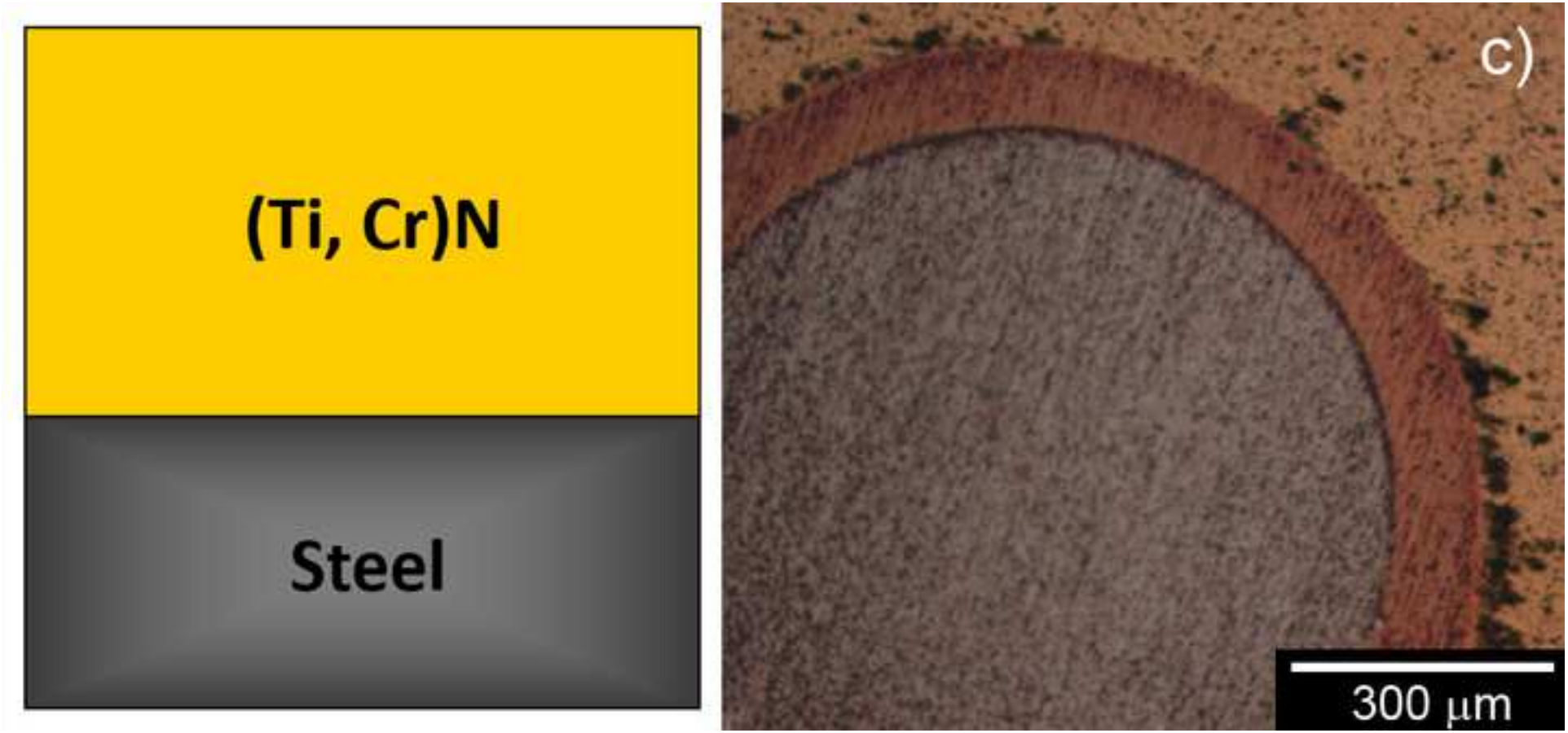

Figure 2

Click here to download high resolution image

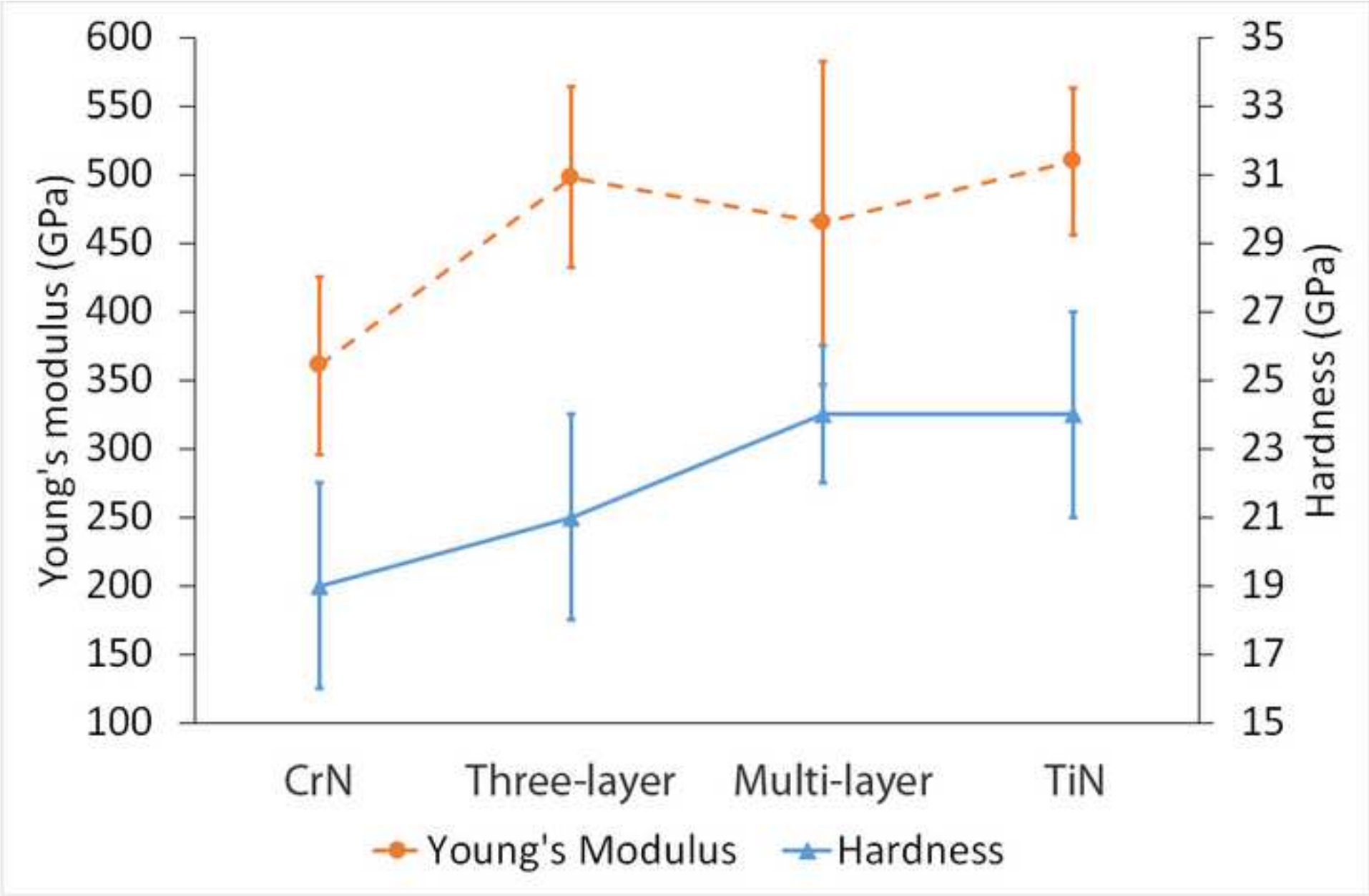

Figure 3
Click here to download high resolution image

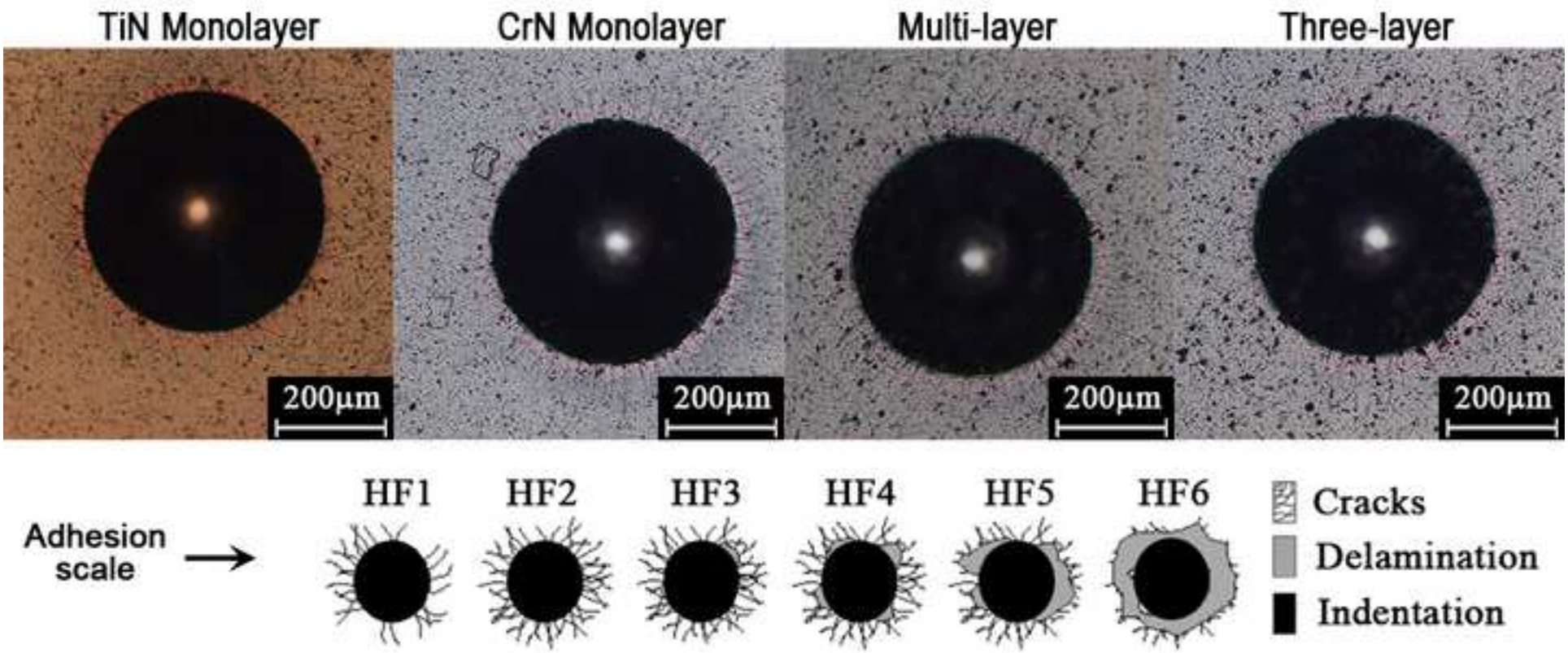

Figure 4

Click here to download high resolution image

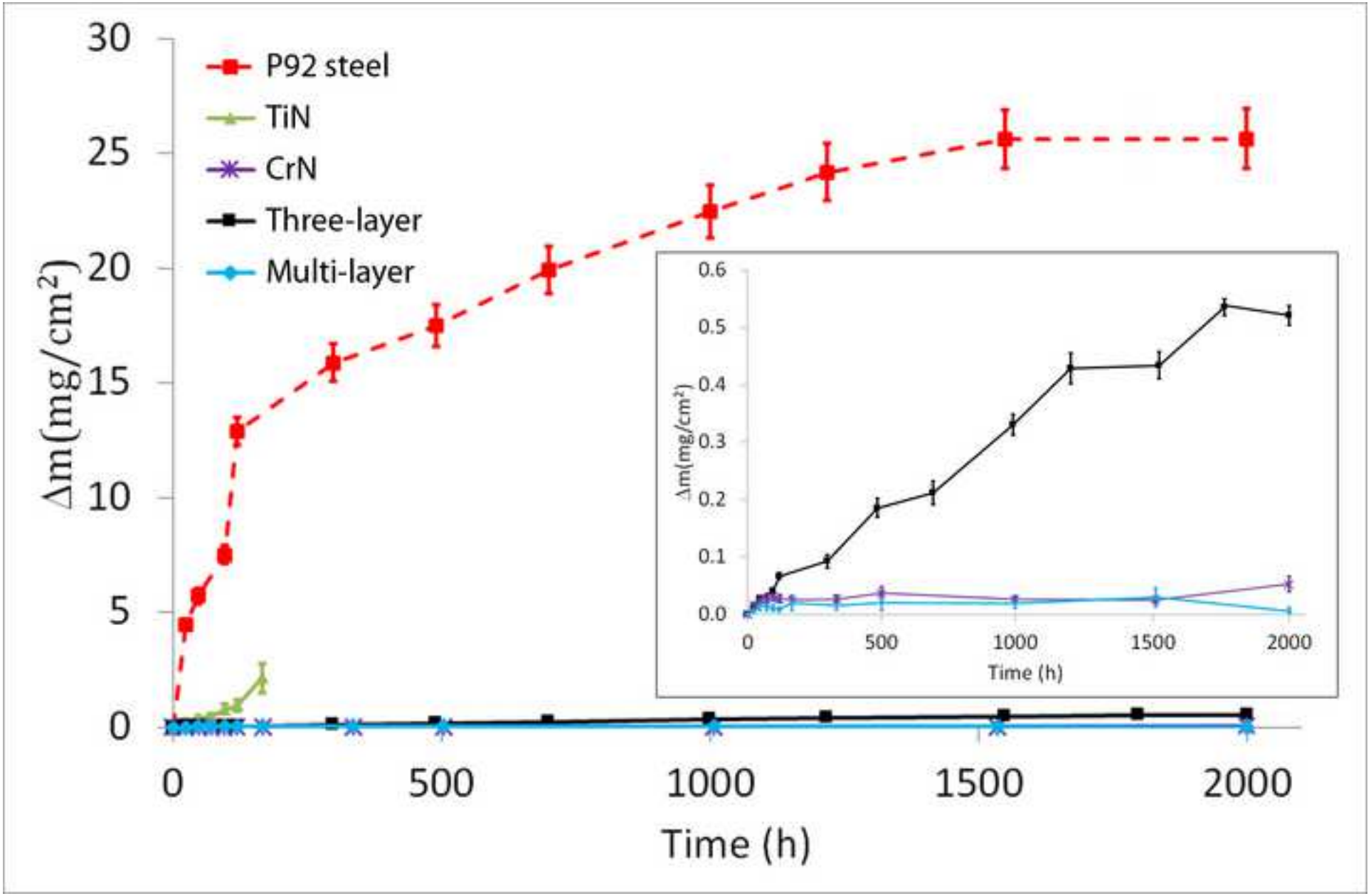

Figure 5a

Click here to download high resolution image

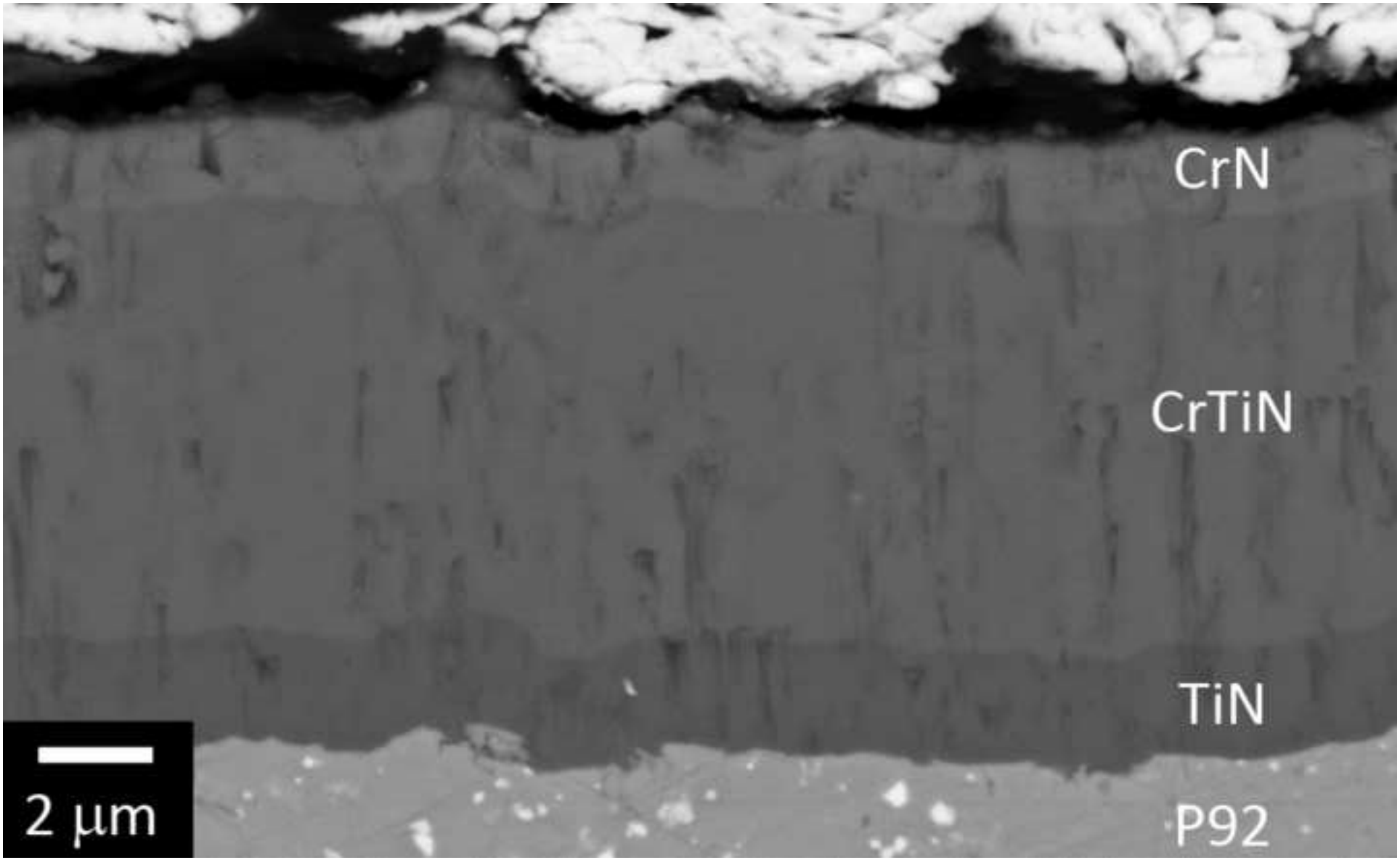

Figure 5b

Click here to download high resolution image

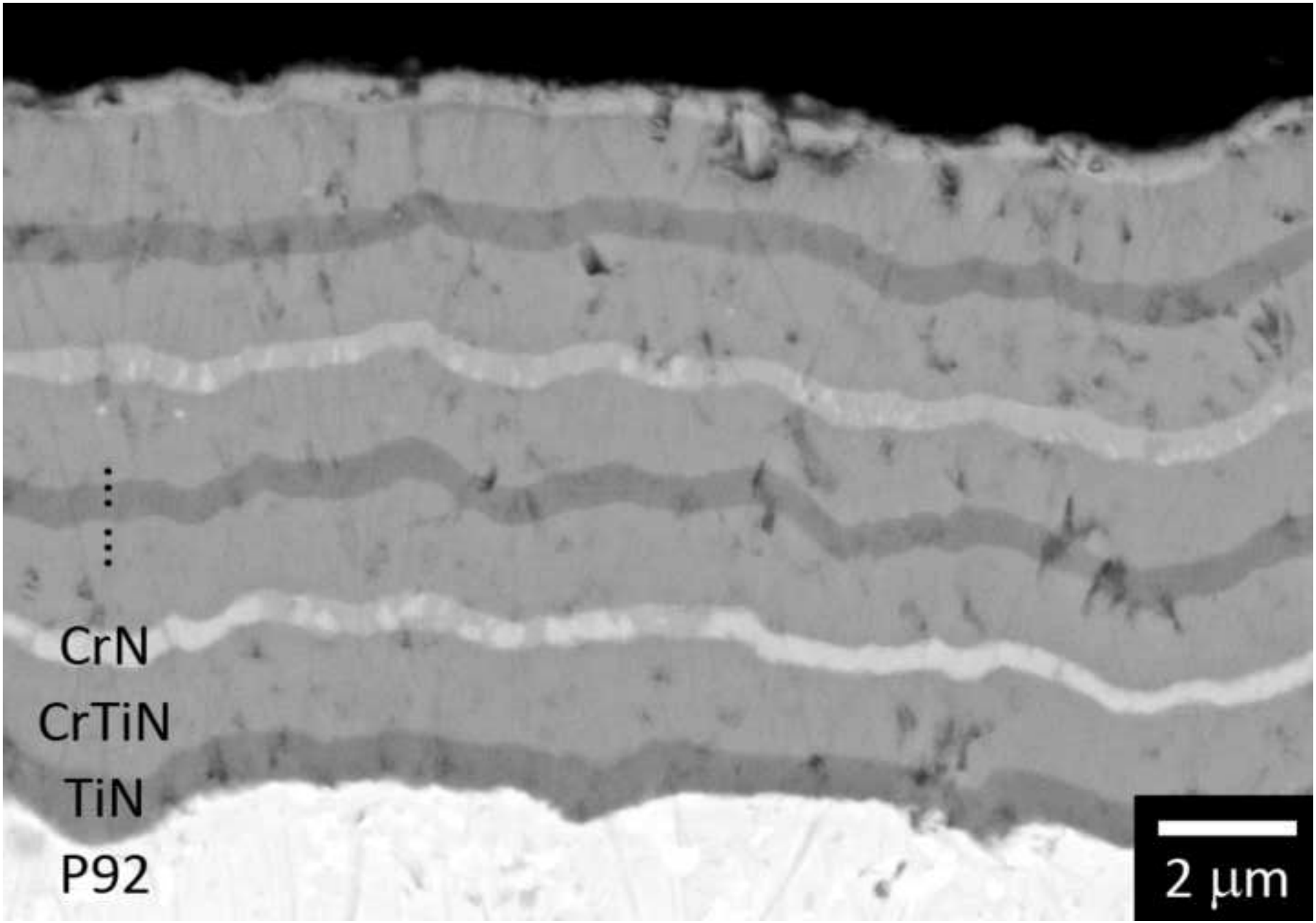

Figure 6a
Click here to download high resolution image

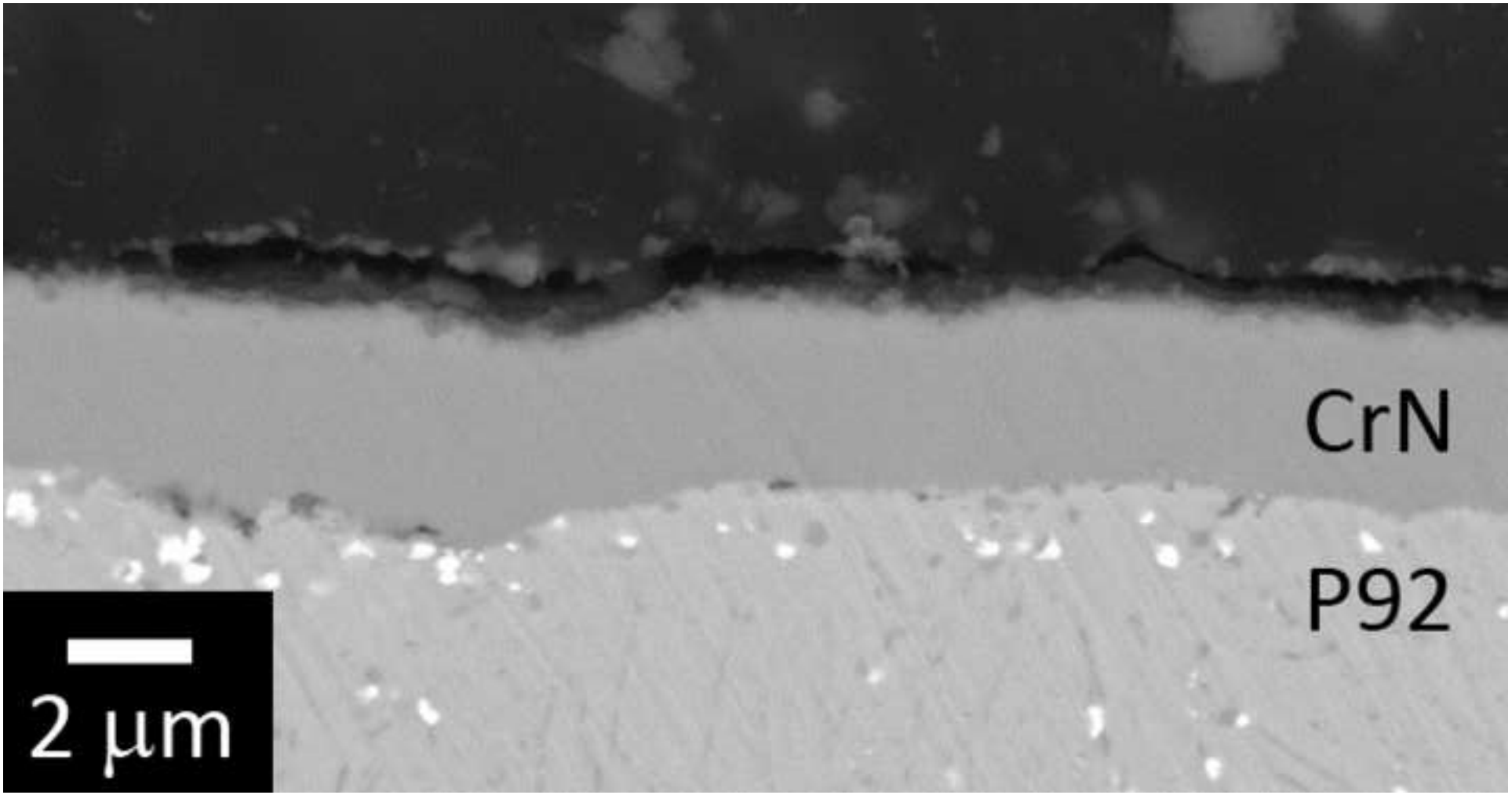

Figure 6b

Click here to download high resolution image

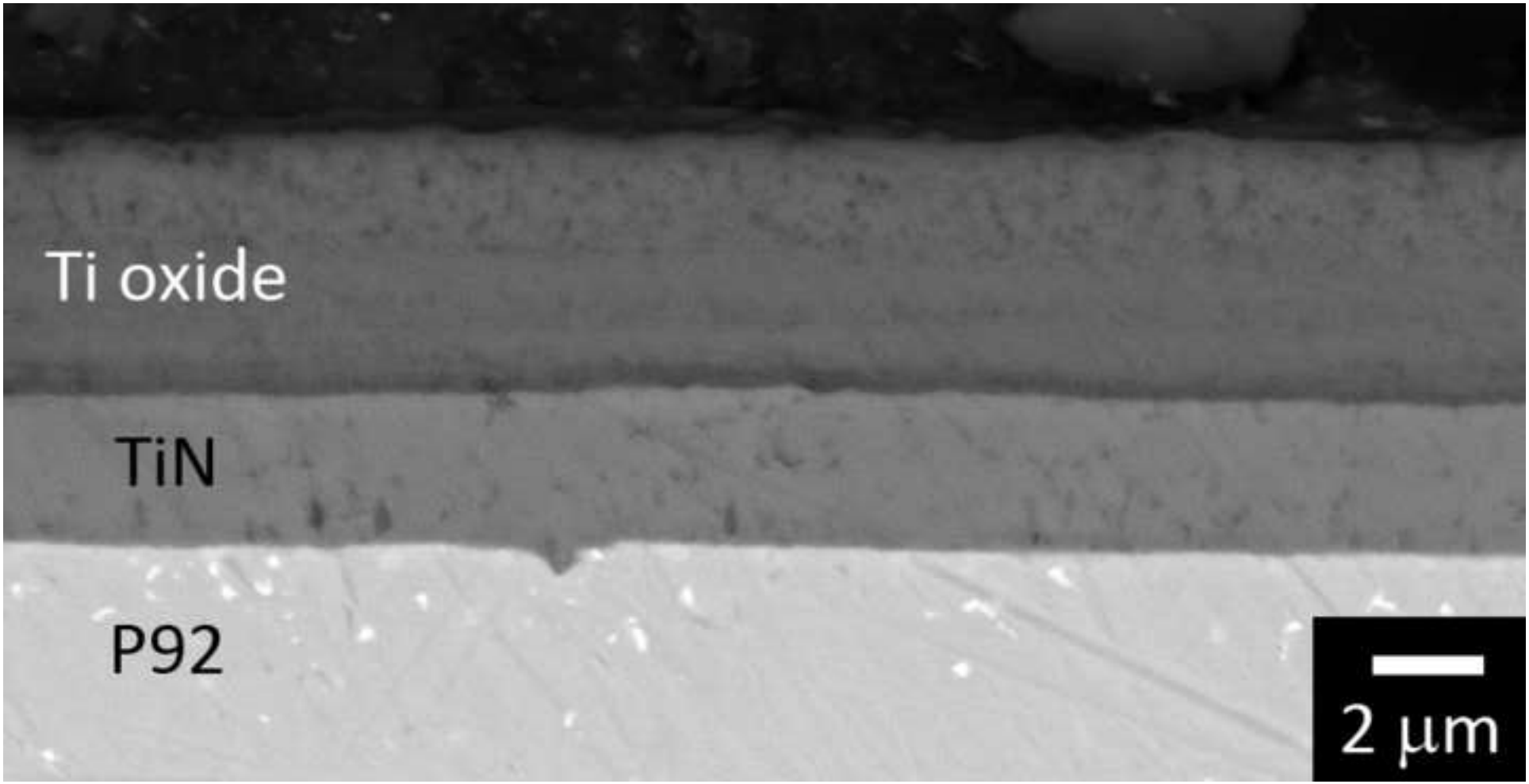

Figure 7a

Click here to download high resolution image

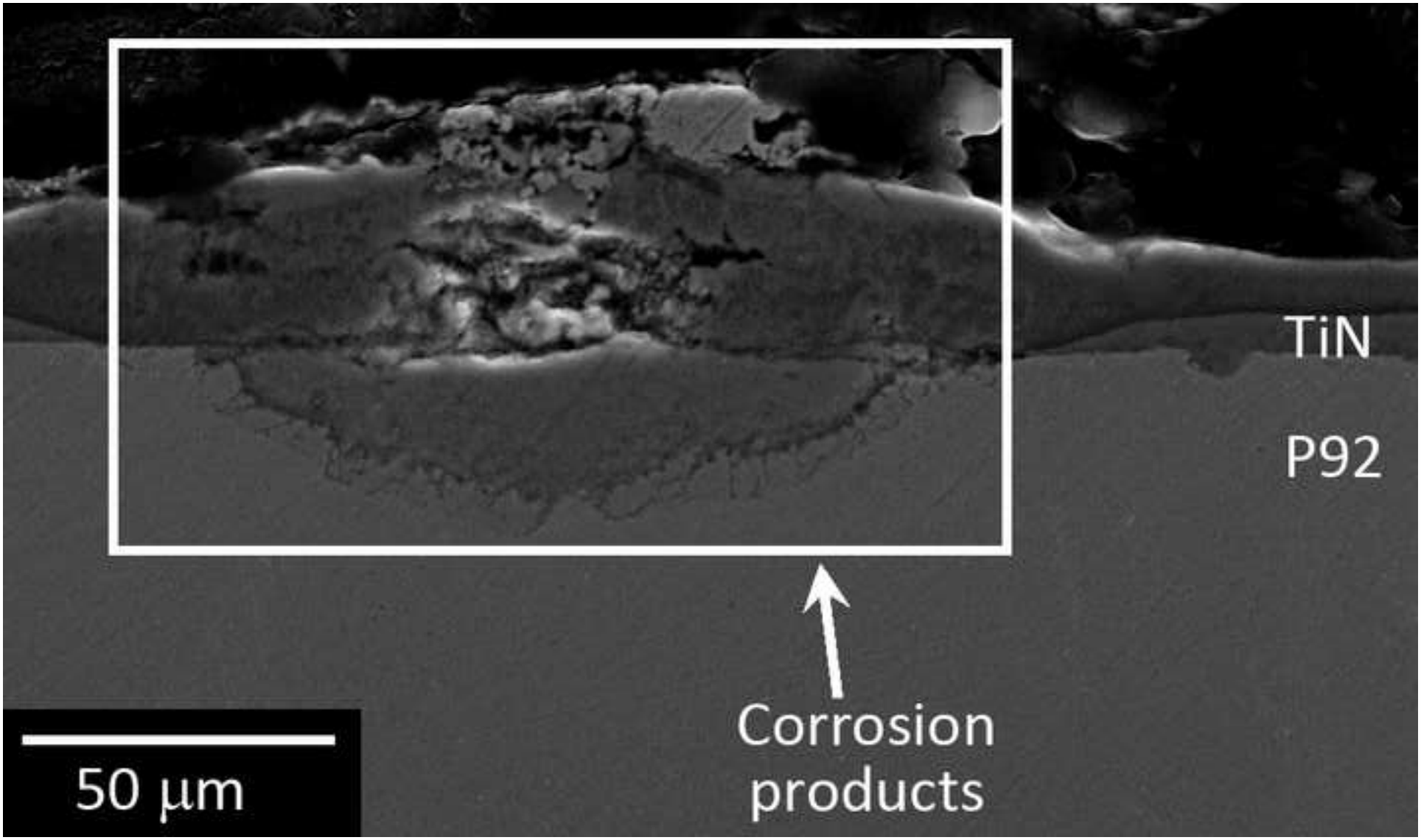

Figure 7b

Click here to download high resolution image

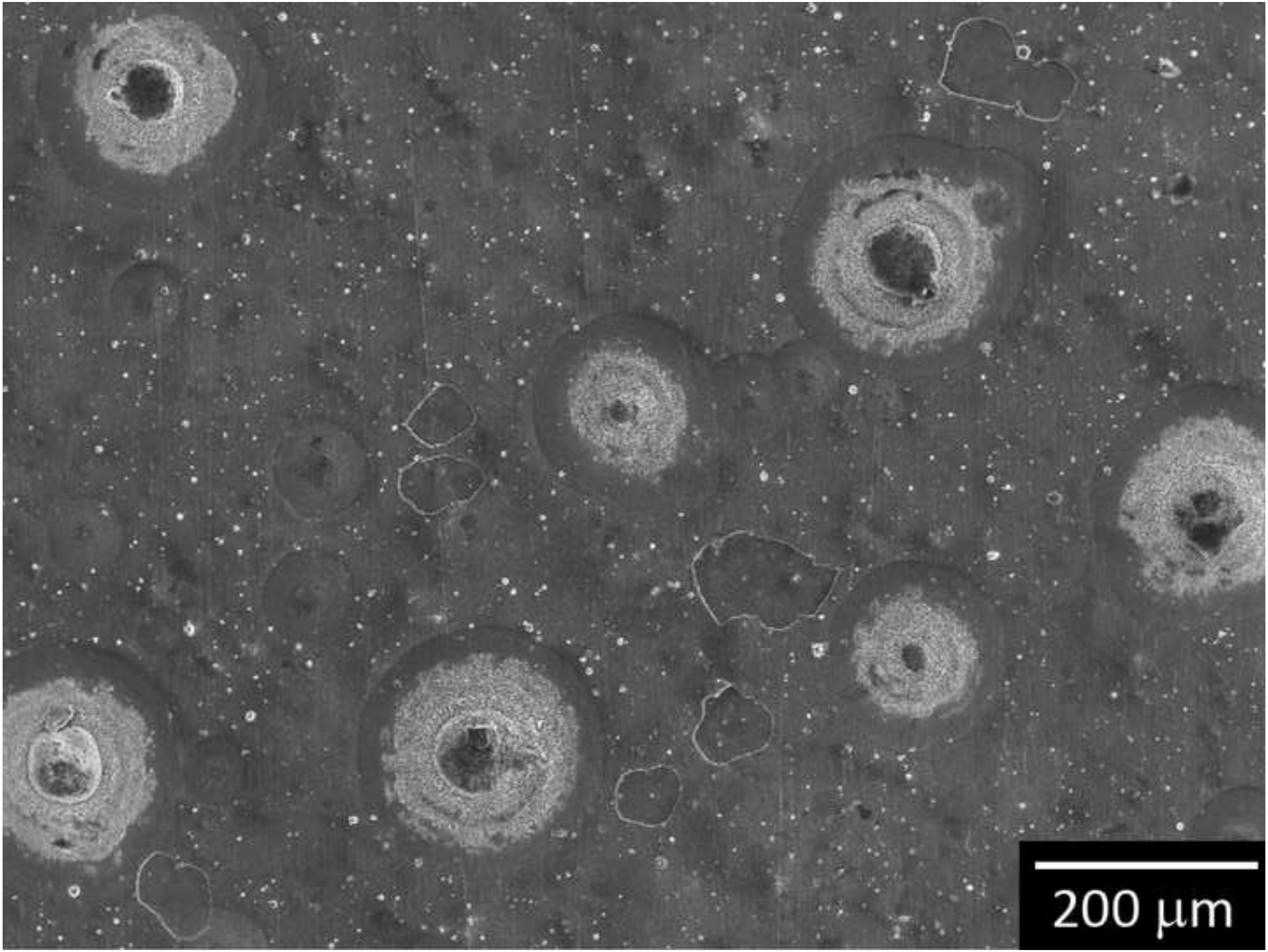

Figure 8ab

Click here to download high resolution image

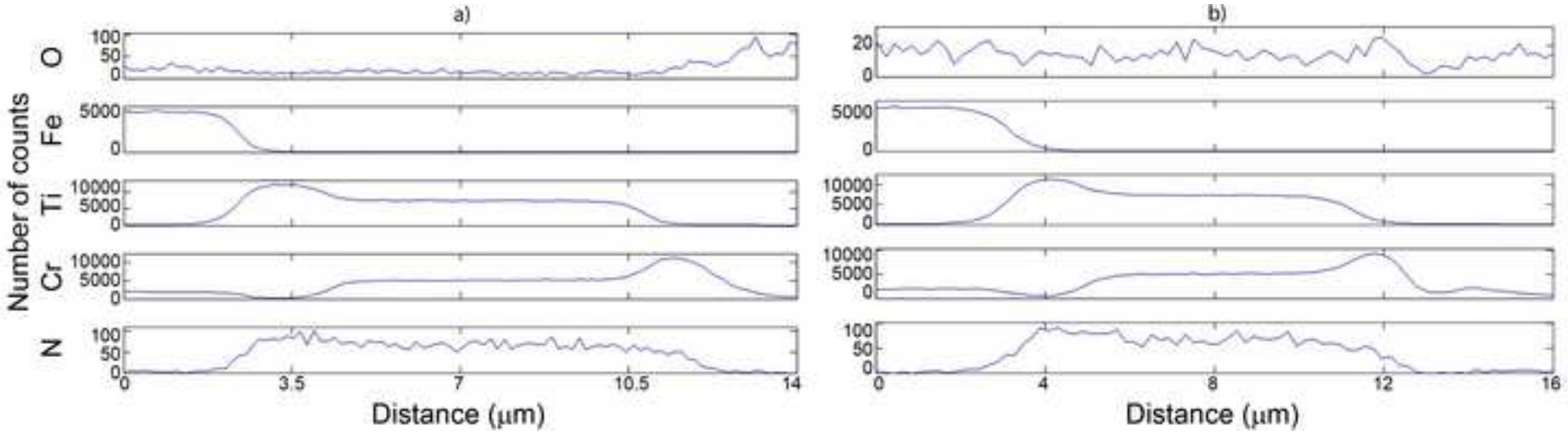

Figure 8cd

Click here to download high resolution image

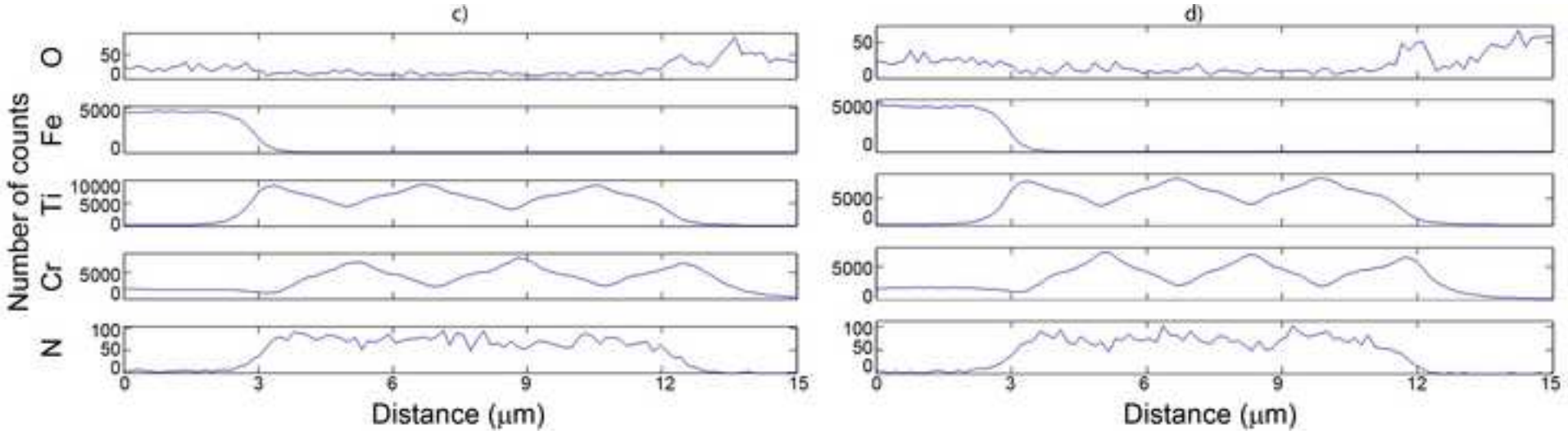

Figure 9a

Click here to download high resolution image

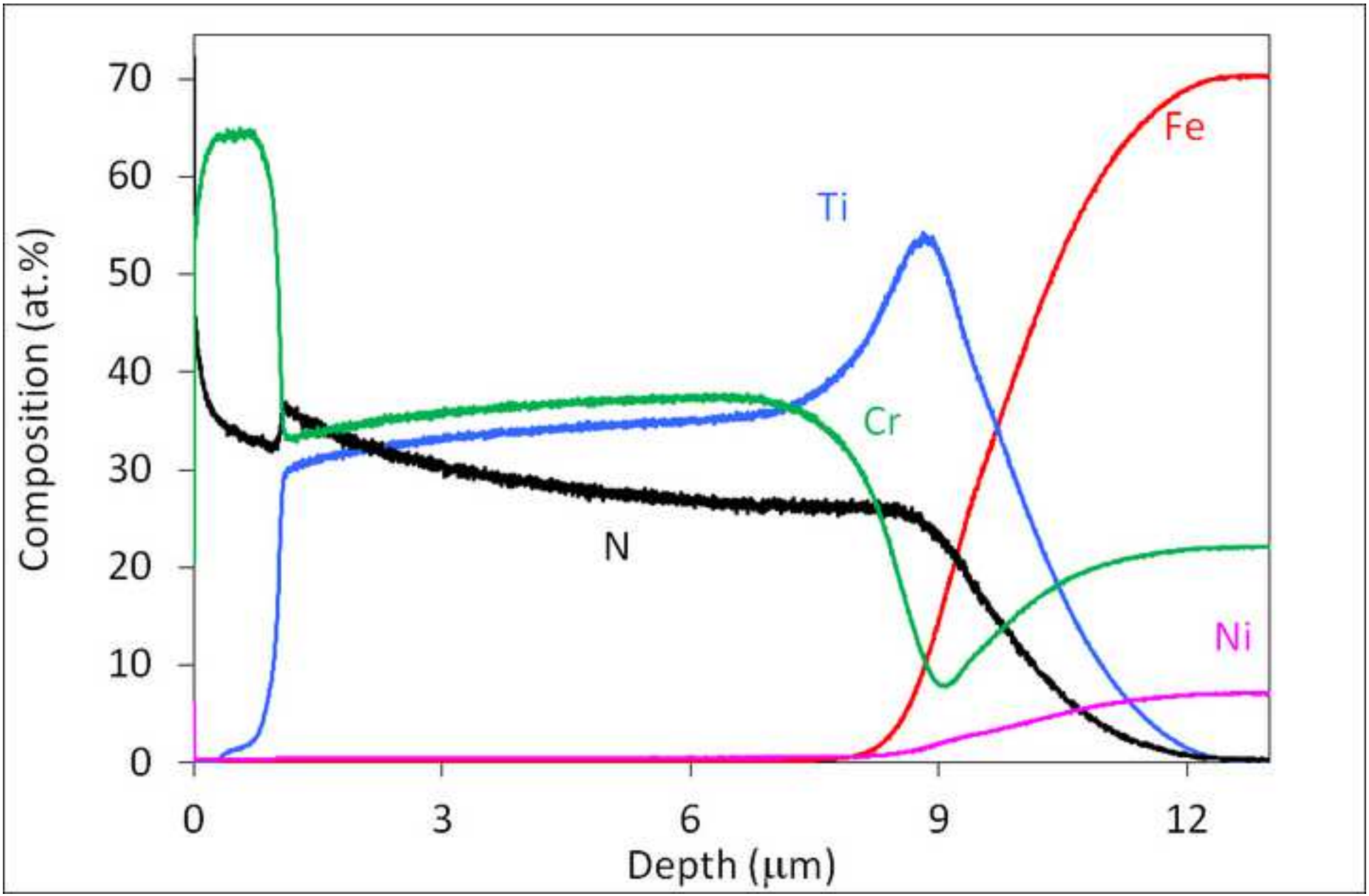

Figure 9b

Click here to download high resolution image

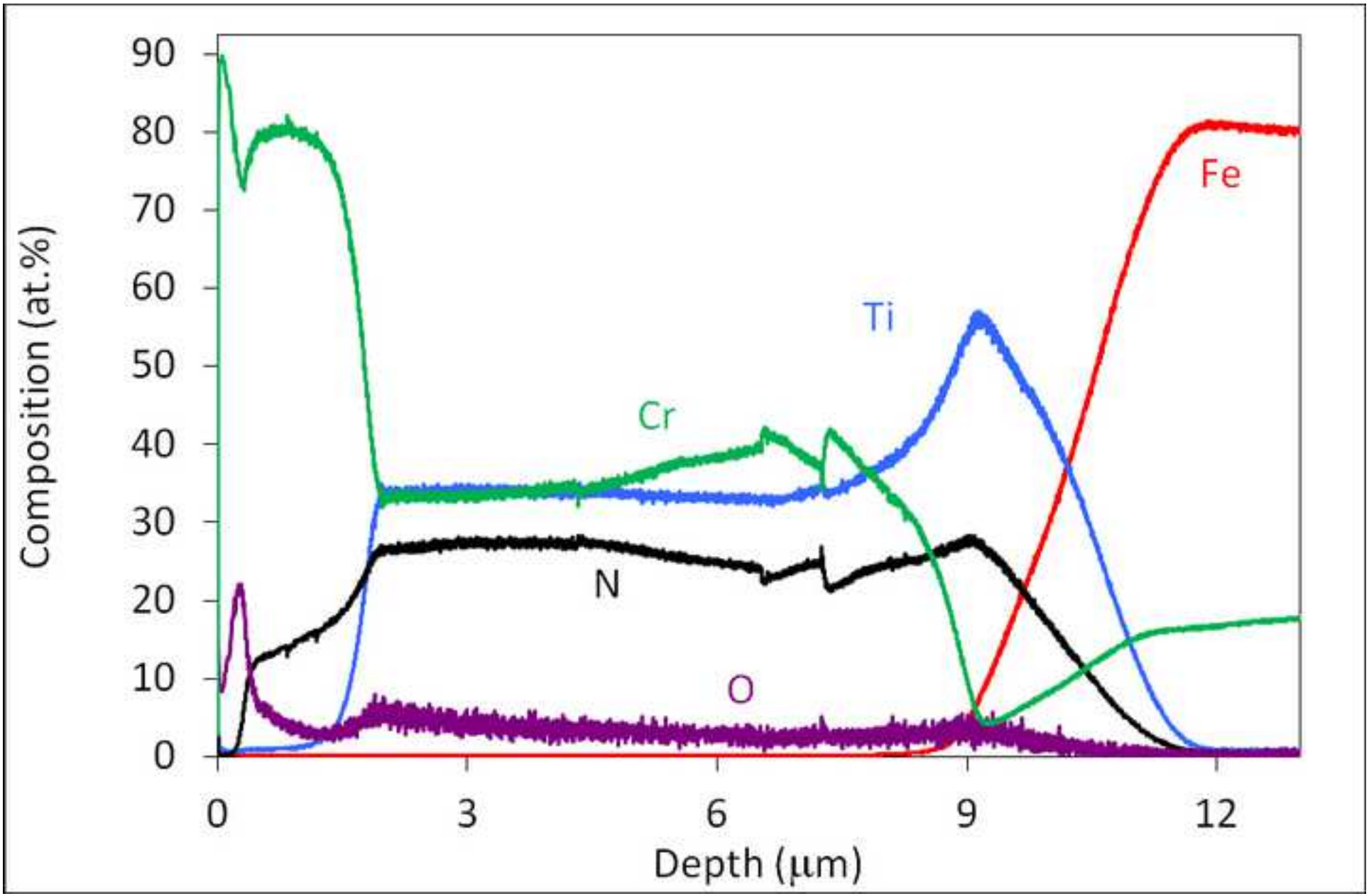

Figure 9c
Click here to download high resolution image

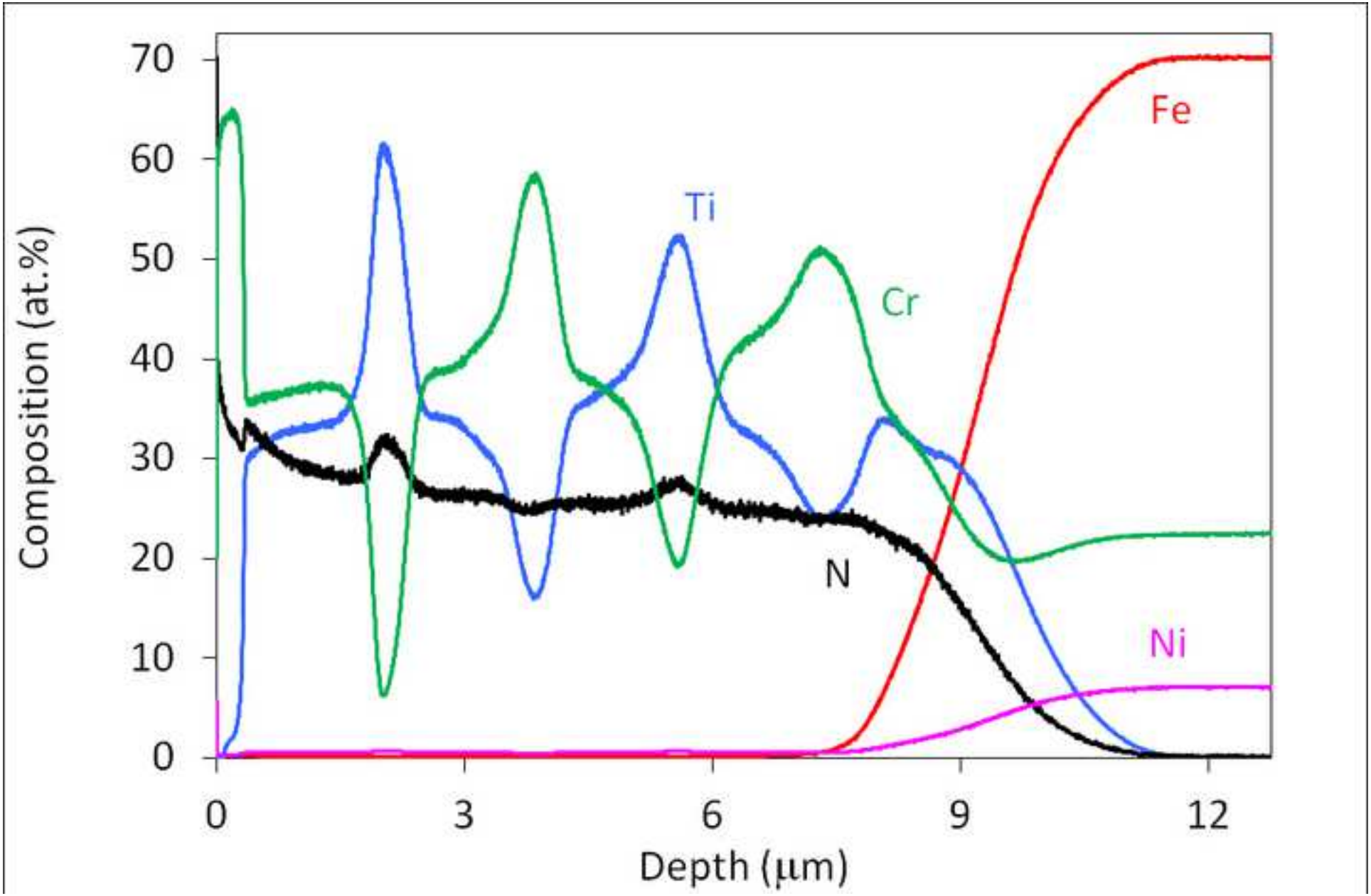

Figure 9d

Click here to download high resolution image

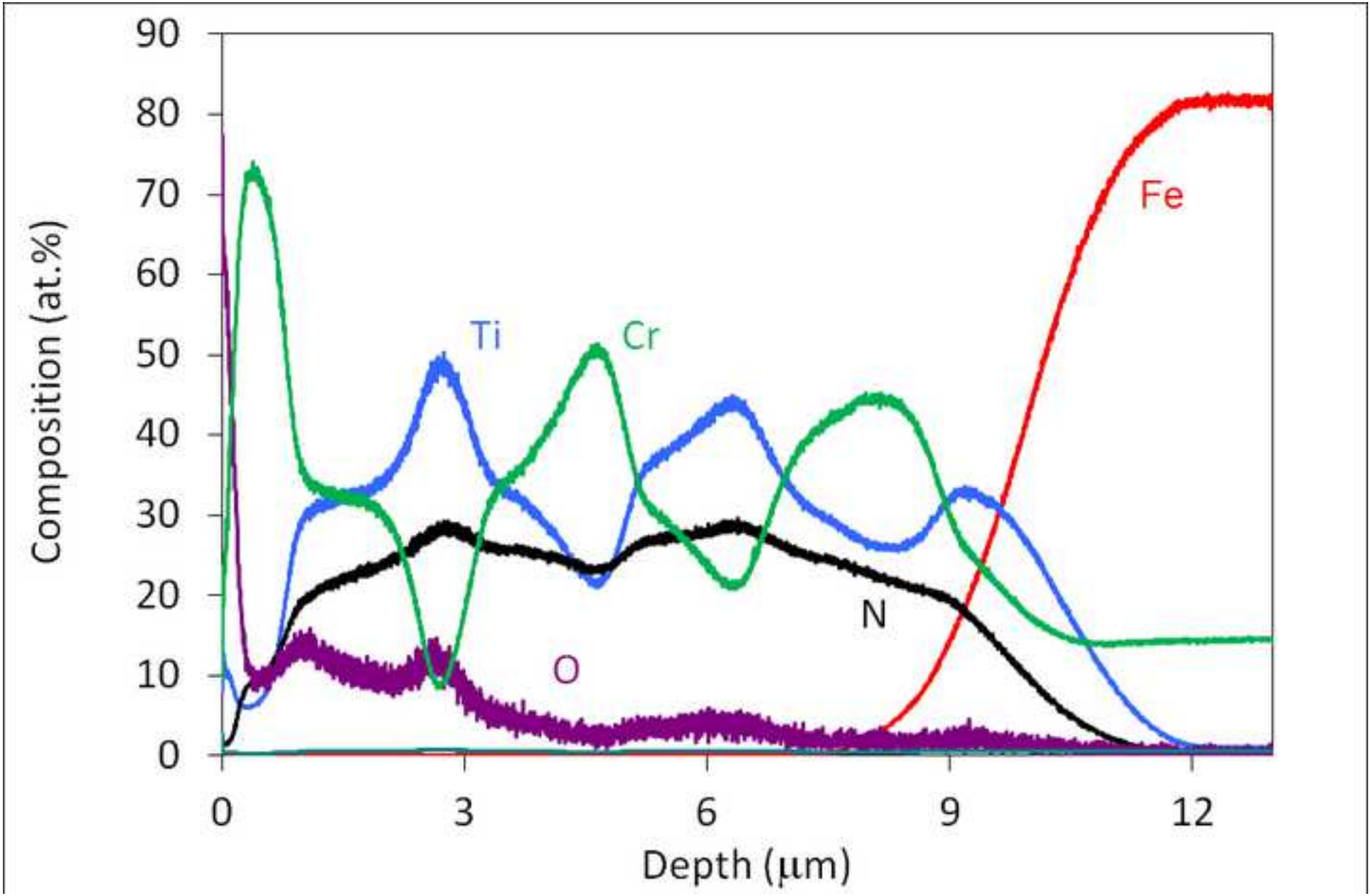

Figure 10a

Click here to download high resolution image

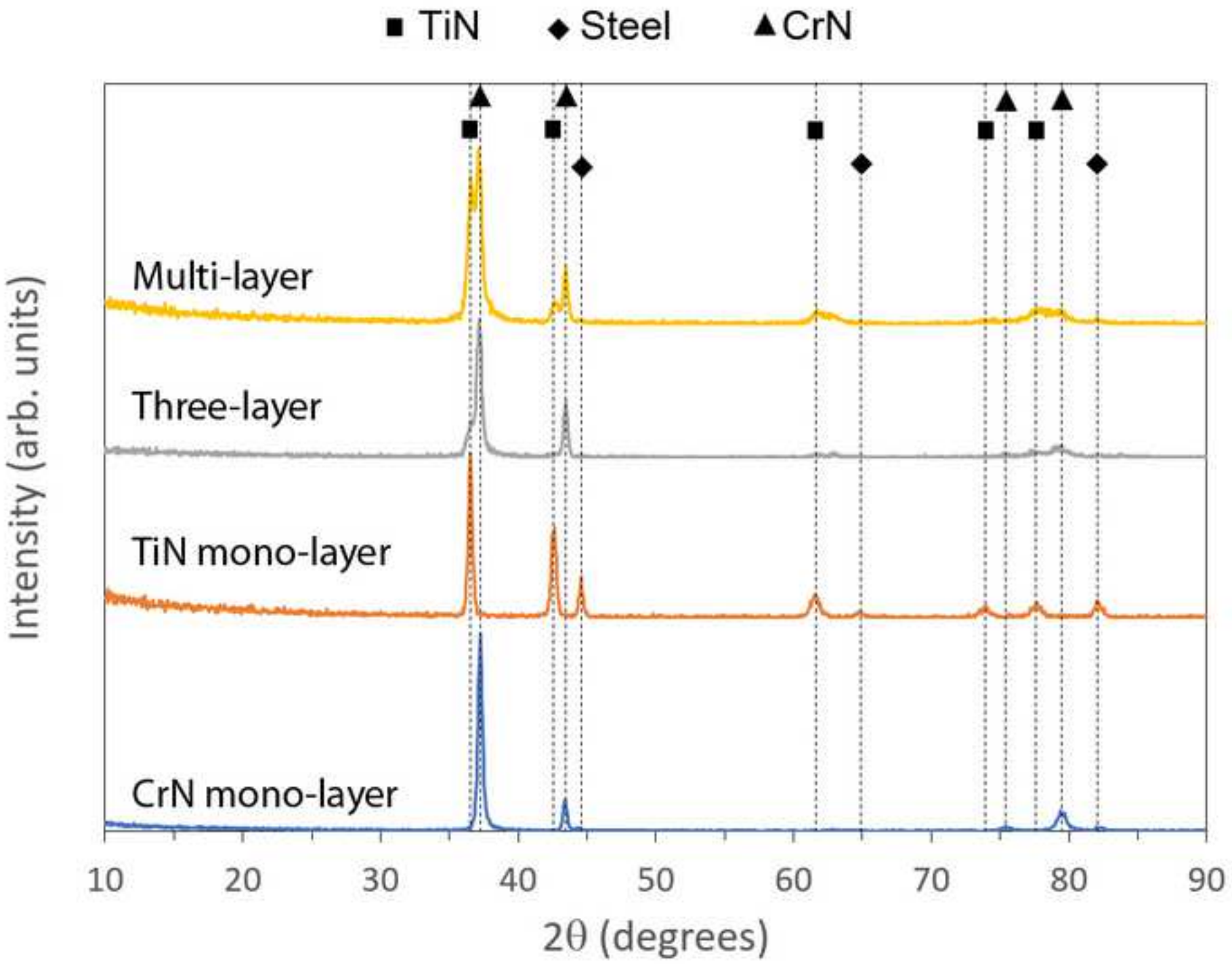

Figure 10b

Click here to download high resolution image

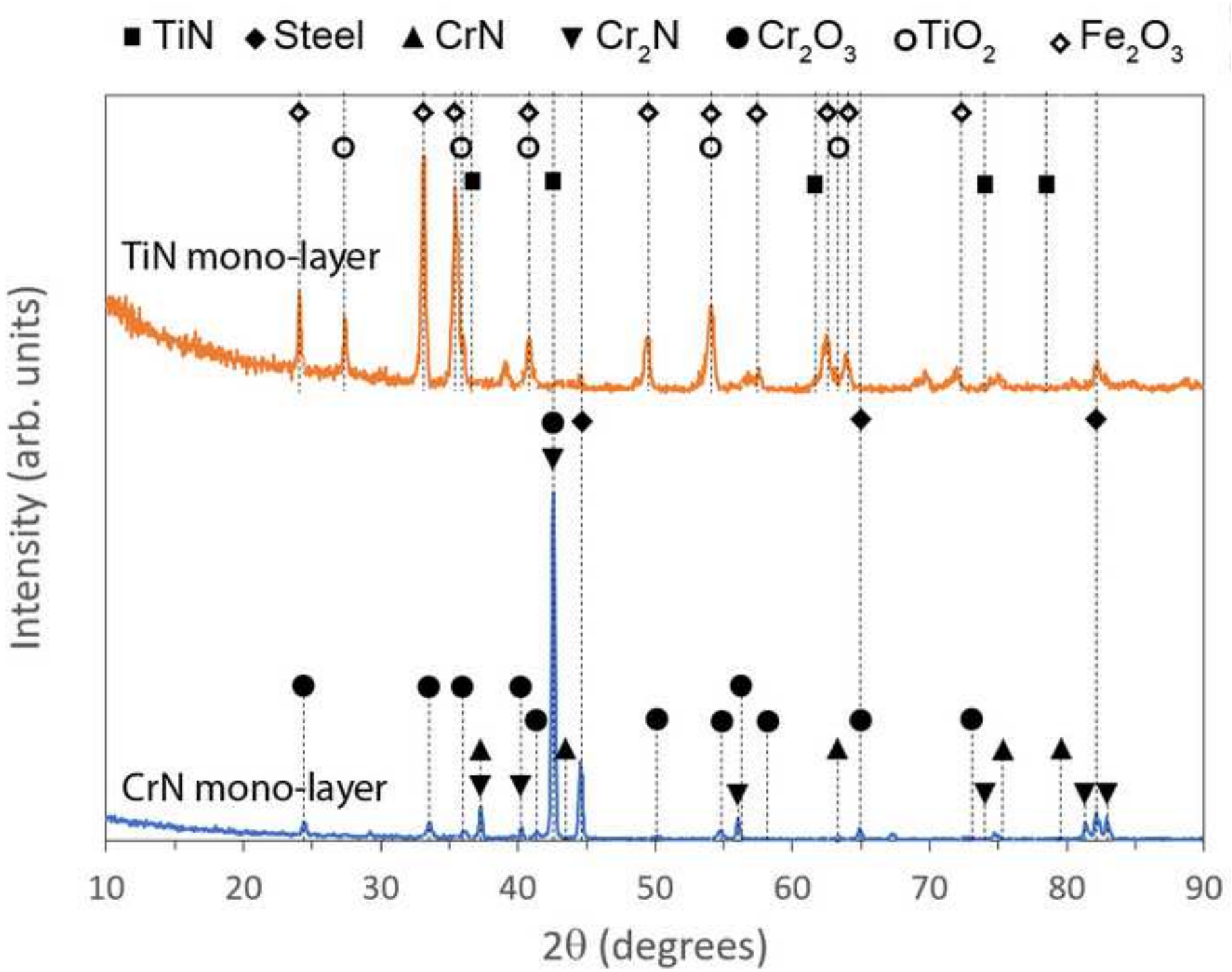

Figure 10c

Click here to download high resolution image